# Stony Brook University

# Experimental Study of Crack Propagation Characteristics in Lamellar TiAl

**A Thesis Presented**

**by**

**Gunes Uzer**

**to**

**The Graduate School**

**in Partial Fulfillment of the**

**Requirements**

**for the Degree of**

**Master of Science**

**in**

**Mechanical Engineering**

**Stony Brook University**

**August 2007**

**Stony Brook University**

The Graduate School

GUNES UZER

We, thesis committee for the above candidate for the

Master of Science degree, hereby recommend

Acceptance of this thesis

Dr. Fu-pen Chiang – Advisor
Mechanical Engineering Department

Dr. Chad Korach– Chair
Mechanical Engineering Department

Dr. Toshio Nakamura – Member
Mechanical Engineering Department

This thesis is accepted by the graduate school

Lawrence B. Martin
Dean of the Graduate School

Abstract of the Thesis

# Experimental Study of Crack Propagation Characteristics in Lamellar TiAl

by

Gunes Uzer

Master of Science

in

Mechanical Engineering

Stony Brook University

2007

ESP (Electron Speckle Photography) is a micro/nano experimental mechanics technique. It is capable of performing full field displacement mapping over a region of only several microns in diameter.

In this dissertation, ESP is applied to the investigation of the crack propagation characteristics of lamellar TiAl with the grain size of approximately 450μm. A narrow coupon specimen with a single edge crack and circular disks of about 1mm in thickness and 3.5mm to 9mm in diameter are manufactured and uniaxial tension and Brazilian tests are performed inside the Hitachi S2460N electron microscope. The specimens were gradually loaded under incremental forces and the SEM image was taken at each step of the loading until they failed. The displacement and strain fields were measured using the

technique of Computer Aided Speckle Interferometry (CASI). The analysis of data shows that the lamellar orientation and grain boundary of TiAl play major roles in the characteristics of crack propagation. The highest resistance to crack advance is when the crack is normal to the lamellar orientation whereas the weakest link is when the interface is parallel to the orientation of the crack. Moreover, we find that a concentrated strain field tends to be the prelude of a sudden crack jump. The shear strain also plays an important role in crack advance by shear banding. And crack Propagation in TiAl is always in mixed mode regardless of loading condition.

*Dedicated to my family*

# *TABLE OF CONTENTS*


DEDICATION ..... V

TABLE OF CONTENTS ..... VI

LIST OF FIGURES ..... VIII

ACKNOWLEDGEMENTS ..... XI

CHAPTER 1 INTRODUCTION ..... 1

1.1 State of the Art & Scope of the Research ..... 1

CHAPTER 2 ELECTRON SPECKLE PHOTOGRAPHY (ESP) ..... 4

2.1 Introduction ..... 4

2.2 Evolution of Optical Speckle Techniques ..... 6

2.2.1 Laser Speckle Technique ..... 6

2.2.2 White Light Speckle Technique ..... 9

2.2.3 Digital Speckle Technique ..... 10

2.3 Electron Speckle Photography (ESP) ..... 13

CHAPTER 3 APPLICATION OF ESP TO EXPERIMENTAL STUDY OF CRACK PROPAGATION CHARACTERISTICS IN LAMELLAR TIAL ..... 15

3.1 Testing System ..... 15

3.2 Materials and Specimen Preperation ..... 17

3.3 Experimental Study of Crack Propagation Characteristics under Mode I Loading ..... 19

3.4 Experimental Study of Crack Propagation Characteristics under Mixed Mode Loading..... 27

3.5 Discussion and Conclusions..... 38

BIBLIOGRAPHY..... 47

# *LIST OF FIGURES*

Figure 2.1 A typical laser speckle pattern..... .5

Figure 2.2 Pointwise filtering of specklegram.....7

Figure 2.3 Full field filtering of specklegram.....9

Figure 2.4 A typical white light speckle patter Laser Speckle Pattern..... 10

Figure 2.5 Schematic of CASI for Calculating Displacement Vectors..... 12

Figure 3.1 A The Uniaxial Tensile Loading Device.....16

Figure 3.2 Optical & SEM Micrographs of Polycrystalline Lamellar TiAl..... 17

Figure 3.3 Geometry of SEN specimen, (b) initial crack generated by fatigue,
(c) initial crack with larger magnification..... 20

Figure 3.4 Load-extension history of a crack in a simple
tension specimen with a single edge notch.....21

Figure 3.5 Crack extension as a function of load and the crack tip position ant 22.2 N... 22

Figure 3.6 The secondary crack jumped across grain boundary..... 23

Figure 3.7 Slow crack growth period between P = 326.9 N. and P = 433.7.....24

Figure 3.8 Slow Crack Growth Period between P = 459 N and P = 480.8 N.....25

Figure 3.9 Slow crack growth period between P = 326.9 N and P = 433.7 N.
Crack tip tries to align itself with the grain orientation.....26

Figure 3.10 Geometry of the cracked Brazilian disc test specimen..... 27

Figure 3.11 Figure 3.16 Displacement fields of a 9 mm
Brazilian disk under compression prior to crack initiation.....28

Figure 3.12 Displacement fields of specimen B prior to crack Initiation.

(a) U-field (b) V-field..... 30

Figure 3.13 Two cracks appear at the ends of the central slot

of the 7mm Brazilian disc.....31

Figure 3.14 Crack tip deformation fields and location..... 32

Figure 3.15 Displacement fields of specimen C prior to crack initiation.

(a) U-field (b) V-field. (c) crack after Initiation..... 34

Figure 3.16 Linkage between two cracks via mode II.....36

Figure 3.17 u and v fields prior to crack initiation, (a) u field at 25x,

(b) v field at 100x, (c) u field at 100x in specimen D.....37

Figure 3.18 Shear strain field prior to the crack jump across grain boundary.....39

Figure 3.19 Superposition of shear stress field prior to crack jump with the trace of the

jumped crack….....40

Figure 3.20 Displacement fields of specimen C prior to crack initiation. (a) u-field

(b) v-field.(c) εxx strain field.(d) crack initiated in the site indicated by strain field

(Shown by the red arrow)..... 41

Figure 3.21 Strain field surrounding the crack tip between P= 400.7 N and P= 450.6 N. 35

Figure3. 22 Mode I failure is the dominant failure mode irrespective of the

initial Slot orientation..... 44

Figure3.23 Evaluation of mode mixity on CBD specimen.....46

# *ACKNOWLEDGEMENTS*

I am deeply indebted to my advisor, Professor Fu-Pen Chiang for his unending guidance and support. Advice from him has extended far beyond the technical realm. It is my tremendous honor to complete this research work under his supervision..

My sincere appreciation is extended to Professor Chad Korach and Professor Toshio Nakamura for supporting my research and reviewing this work.

I wish to express my gratitude to all my friends and colleagues who have supported my effort in graduate study and academic research in the department of Mechanical Engineering.

I would like to thank my family. Without my parent's encouragement, it would have been impossible for me to accomplish this work.

Finally, Funding provided by the Air Force Office of Scientific Research via grant# F49620-03-0282 greatly appreciated. In particular Special thanks are due to Dr. Craig S. Hartley, Dr. Jaimie S. Tiley and Capt. Brett P. Conner, the program directors.

# Chapter One:

# Introduction

## 1.1 State of the Art & Scope of the Research

Two phase titanium aluminide (TiAl) alloys are potential materials for new high efficiency aerospace applications. They attracted great deal of attention from aerospace community during last decade. TiAl alloys with fully lamellar microstructures are one of the potential candidates for next generation jet engine blades. This is essentially due to attractive properties of lamellar TiAl such as low density, oxidation resistance, high resistance to fracture and maintaining strength at high temperatures (Dimiduk et al, 1995). Based on a concentration of Al and heat-treatment processes, TiAl alloys assume different micro-structural properties (Kim, 1994). Al concentrations range from ~%46 to ~%56 with additions of V, Cr, Nb, W, Ta, B which about %3 (Appel and Wagner, 1998). Microstructure of lamellar TiAl consists of randomly oriented grains of two phases TiAl ($\gamma$) and $Ti_3Al$ ($\alpha_2$). Orientation relationships between these two phases are $(111)_\gamma \,||\, (0001)_{\alpha_2}$ and $< 1\bar{1}0]_\gamma \,||< 11\bar{2}0 >_{\alpha_2}$ (Sastry and Lipsit, 1977; Feng et al., 1988). Platelets inside the grain are not ordered like $\gamma/\alpha 2$ pairs, typically volume fraction of $\gamma$ platelets are higher (Arata et al., 2000)

Mechanical properties of TiAl alloys investigated during recent years including single phase PST crystals (Inui, Nakamura and Yamaguchi, 1992), duplex structures

(Kim, 1994), nearly lamellar structures with partial duplex structure (Chan and Kim, 1992) and two phase fully lamellar structures (Chan and Shih, 1996; Arata et al., 2000) Among these only two phase lamellar TiAl alloys appear to be successfully advancing toward structural applications within the next decade. Two phase fully lamellar structures found to have higher fracture toughness and stable crack growth when compared with nearly lamellar or duplex structures (Dimiduk et al., 1995; Kim, 1994; Kim, 1995). Fracture toughness of two phase TiAl alloys in lamellar form has been known to increase with increasing the size of lamellar grains, on the contrary the ductility decreases with increasing the lamellar grain size (Dimiduk et al., 1998; Kim, 1994 ). Fully lamellar microstructures consisting of large lamellar grains result in poor tensile properties. This can be improved by refining their lamellar structures however, at the same time their fracture properties deteriorate. Failure behavior of TiAl is important in engineering applications.

Studies dealing with the questions of microstructural effects on crack propagation mainly utilized the use of electron microscopy (Scanning electron microscopy (SEM), or transmission electron microscopy (TEM), Scanning Tunneling Microscopy (STEM), etc...). It is found that the fracture process in two phase lamellar TiAl alloy occurs primarily by crack propagation in the interlamellar direction, crack extension occurs by nucleation of microcracks and formation of interconnecting ligaments ahead of the main crack (Chan et al., 2000). Although observations made by electron microscopy, not many studies used high resolution full field deformation techniques. One of them was machine –vision based stereo-imaging technique DISMAP (measurements of micro displacements by machine vision photogrammetry) (Franke, Wnezel and Davidson, 1991). The accuracy

of this technique depends on many factors, such as texture of surfaces from which measurements are made, resolution of photographs and their alignment in the measuring system. Among them surface nature is the most important factor. A desired specimen surface “must be created that has numerous fine features” (Franke, Wenzel and Davidson, 1990). Obviously, it is impossible for naturally existed features in material to satisfy this requirement in different magnification and length scales.

The aim of this work is to use Electron Speckle Photography (ESP) technique to study propagation characteristics of TiAl with fully lamellar structure. The thesis is organized in three chapters, starting from the evolution of speckle technique, principle of ESP technique is described and its development is briefly reviewed.

In Chapter 3 available testing system including special designed loading stage and scanning electron microscope (SEM) are briefly described. Application of ESP technique consists of three parts; creating micro/nano speckles that are used as gaging devices on the surface of the specimen, recording speckle patterns using SEM and analyzing speckle images by CASI (Computer Aided Speckle Interferometry). In this section creating micro/nano speckles described together with materials used and specimen preparation. Finally the crack propagation for the mode I and mixed mode specimens described.

# Chapter Two:

# Electron Speckle Photography (ESP)

## 2.1 Introduction

A speckle is a spot with a certain size, shape and intensity. It is formed by the interference of two or more rays of coherent light reflecting from diffuse surface of a specimen. Thus each point on the object's diffuse surface acts as a light source with rays propagating radially outward in all directions. The unique properties of a specific speckle are due to local microscopic surface imperfections on the specimen. If the surface of the specimen undergoes a deformation speckles move. Figure 2.1 shows a typical laser speckle pattern. Since the speckle pattern is caused by random interference of light, it acts as a grid in all directions printed on the object's surface. By comparing the speckle patterns before and after the deformation, displacements and strain on the surface can be determined.

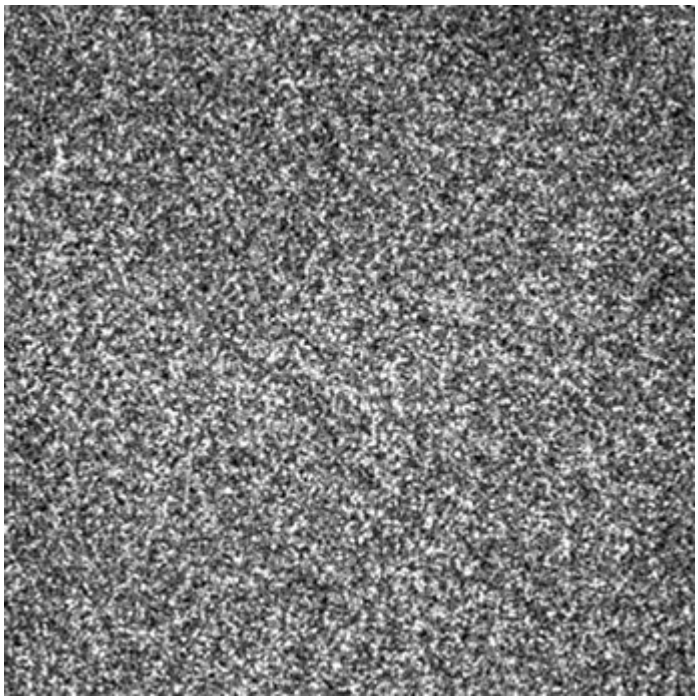

Figure 2.1 A typical laser speckle pattern.

The speckle phenomenon is the basis for two optical methods for measuring displacement, speckle photography and speckle interferometry. In speckle photography displacement measurements made with a speckle pattern created by single illumination beam, this method is also referred as one beam speckle interferometry. It is similar to the moiré method since a speckle pattern can be considered as a grid in all directions. Speckle interferometry is different in a way that deformation is determined by phase difference of two beams of coherent light. It is also referred as two beam speckle interferometry.

Speckle interferometry provides many advantages. One of them is that the resolution of full-field deformation measurement is limited by your recording system. Thus when combined with electron microscopy and digital image processing, it can measure the deformation fields in microscopic scales. Electron Speckle Photography

(ESP) technique is the latest stage in speckle methods. In this chapter, evolution of speckle methods and development of ESP technique are described.

## 2.2 Evolution of Optical Speckle Methods

### 2.2.1 Laser Speckle Technique

Laser speckle technique is highly sensitive and non-destructive. It can be applied to either in-plane or out-of-plane displacement measurements. It can also be used in vibration studies.

Unlike what is observed in the moiré technique, no fringes will result directly upon the superposition of two speckle patterns. The hidden information of displacement has to be extracted by optical Fourier processing. Optical filtering is essentially a process of selecting a particular pitch and grating from a random speckle pattern (Chiang, 1978). It can be done in either full-field or pointwise fashion.

Pointwise filtering of a specklegram is schematically shown in Figure 2.2. Specklegram can be created by recording speckle patterns before and after deformations then superimpose them or by recording them onto same film by double exposure. The displacement between two speckle patterns is delineated by sending a narrow laser beam at the points of interest and receiving their corresponding far field diffraction spectrum on a screen.

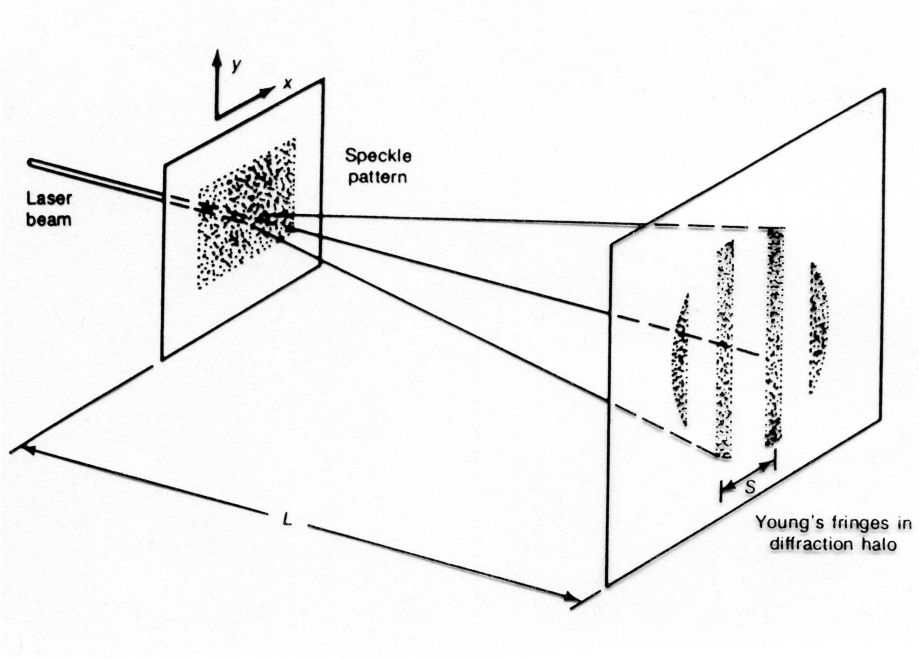


Figure 2.2 Pointwise filtering of specklegram

The observed diffraction halo is modulated by a series of uniformly spaced straight fringes, called Young's fringes. The intensity distribution of the diffraction spectrum is

$$I(\mathrm{u}) = 4\cos^2(k\frac{\mathrm{u}\cdot\mathrm{d}}{2L})I_h(\mathrm{u}) \tag{2-1}$$

where **u** is the position vector at the receiving plane, $k=2\pi/\lambda$ with $\lambda$ being the wavelength of light, **d** the displacement vector at the point of probing, L the distance between the specklegram and the receiving screen and $I_h(\mathbf{u})$ the intensity distribution of diffraction spectrum of a single speckle pattern. Equation (2-1) can be further converted into

$$\mathrm{d} = \lambda L/S \tag{2-2}$$

where d is the magnitude of the displacement vector and S is the fringe spacing. The direction of the displacement vector is perpendicular to the direction of fringes.

The full field filtering is shown in Figure 2.3 (Chiang, 1989). The specklegram is placed inside a convergent laser beam. At the focal plane, a mask with a small hole at **u** is used to block all light except that passing through the small aperture. A second lens is used to receive the filtered light and forms an image of the specimen surface. One sees dark fringes when

$$|\mathbf{d}|\cos\theta = \frac{(n+\frac{1}{2})\lambda L}{|\mathbf{u}|}, n = 0,\pm 1,\pm 2,..., \tag{2-3}$$

and bright fringes when

$$|\mathbf{d}|\cos\theta = \frac{n\lambda L}{|\mathbf{u}|}, n = 0,\pm 1,\pm 2,..., \tag{2-4}$$

where θ is the angle between the displacement vector **d** and aperture vector **u**. These fringes are isothetics, i.e., a loci of points of equal displacement component. Displacement contours along any direction can be obtained by simply varying the direction of the aperture, and the sensitivity of the contour can be changed continuously by sliding the aperture along the direction of the aperture vector.

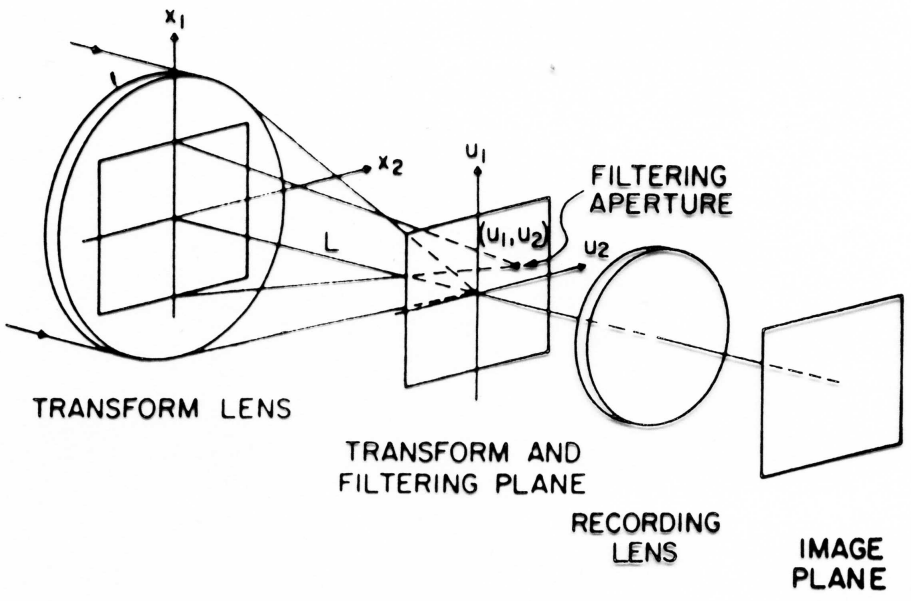


Figure 2.3 Full field filtering of specklegram

### 2.2.2 White Light Speckle Technique

Laser speckle suffers from de-correlation due to factors such as out of plane tilt, large strain, etc. Later it was realized that any random intensity distribution can be considered as speckle pattern (Chiang, 1979). Speckle pattern can be naturally present or artificially created. Thus as long as speckles are distinct and have enough contrast any random pattern may be utilized for speckle metrology. These random patterns can be observed using white (incoherent) light and they referred as white light speckles. Figure 2.4 shows a typical white light speckle pattern. When they recorded they can be processed either in point-wise or full-field fashion as described in previous section. White light speckle method is less susceptible to out of plane tilting.

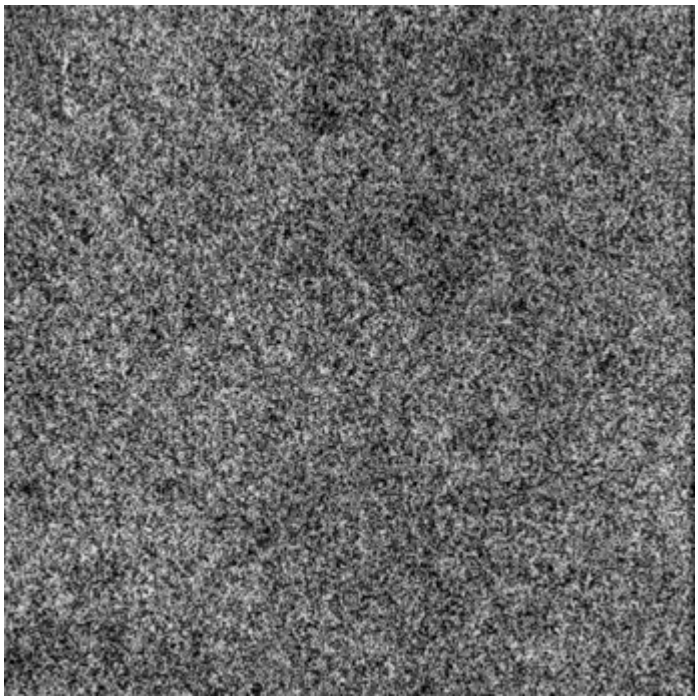

Figure 2.4 A typical white light speckle pattern.

### 2.2.3 Digital Speckle Technique

Digital speckle technique is a very important step in evolution of speckle methods. It keeps all the advantages of the speckle photography but requires neither photograph development nor fringe pattern analysis. In digital speckle method, speckle patterns directly digitized into grey levels and through use of algorithms these patterns can be analyzed. This process can be done either by spatial or spectral analysis.

On the spatial domain, direct speckle correlation methods were developed by constructing a correlation function and defining a correlation coefficient (Peters and Ranson, 1982). The coefficient of least square correlation is

$$C_L = \frac{\iint_A [h_1(x,y) - h_2(x,y)]^2 \, dxdy}{\iint_A h_1^2(x,y) dxdy} \tag{2-5}$$

and the coefficient of cross correlation is

$$C_C = \frac{\iint_A h_1(x,y)h_2(x,y)dxdy}{\sqrt{\iint_A h_1^{\,2}(x,y)dxdy \iint_A h_2^{\,2}(x,y)dxdy}} \tag{2-6}$$

where A is the area of the speckle pattern of interest, $h_1$ and $h_2$ are speckle patterns before and after deformation, respectively, and

$$h_2(x,y) = h_1(x + u_0 + \int \frac{\partial u}{\partial x}dx + \int \frac{\partial u}{\partial y}dy, y + v_0 + \int \frac{\partial v}{\partial x}dx + \int \frac{\partial v}{\partial y}dy) \tag{2-7}$$

When the minimum value of $C_L$ or the maximum value of $C_C$ is reached by changing the displacement components ($u_0$, $v_0$) and the displacement gradients ($\partial u/\partial x$, $\partial u/\partial y$, $\partial v/\partial x$, $\partial v/\partial y$), both displacement and strain are determined. Because the cross correlation function is a strong function of local displacement components but not the gradients and the displacement gradients, calculation is very sensitive to local intensity variations of the image and the use of gradients will introduce some noise to the results.. It is more reliable to perform correlation by searching only two displacement parameters ($u_0$ and $v_0$ not the gradients). The strain fields can be obtained from the differentiation of displacement fields. Nevertheless, since direct speckle correlation involves a huge amount of computation, computation time is very intensive.

On the spectral domain, the correlation technique is CASI (Computer Aided Speckle Interferometry) (Chen, Chiang, Tan and Don, 1993). While it provides a comparable range and sensitivity with the digital speckle correlation, this technique has a much higher computing efficiency. Figure 2.5 illustrates schematically the essence of CASI.

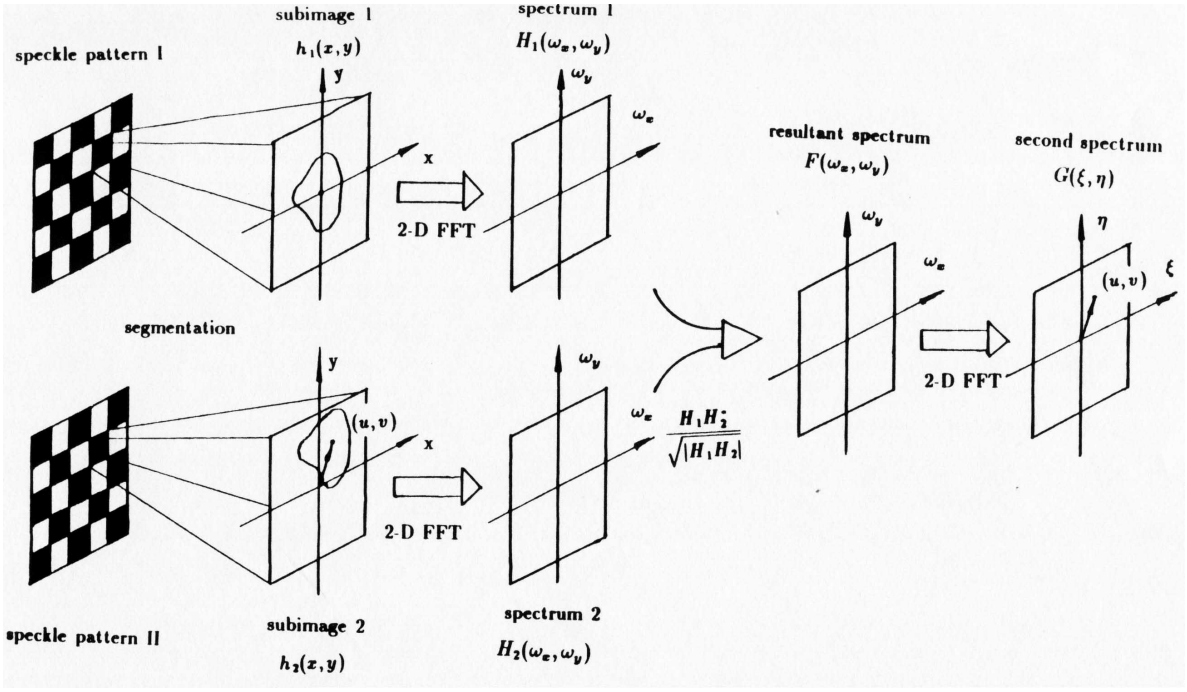


Figure 2.5 Schematic of CASI for Calculating Displacement Vectors

Via CASI, the two speckle patterns are first segmented into set of small subimages. The size of the subimages can be chosen by the user according to different situations. The corresponding subimages are compared with a two-step FFT (fast Fourier transform) process to find the displacement vector.

In Figure 2.5, $h_1(x,y)$ and $h_2(x,y)$ are the complex amplitudes of the light disturbance of a generic speckle subimages, before and after deformation, respectively,

$$h_2(x,y) = h_1[x - u(x,y), y - v(x,y)] \tag{2-8}$$

where $u$ and $v$ are the displacement components along the x and y directions respectively. First step FFT is applied to both $h_1$ and $h_2$,

$$\begin{aligned} H_1(f_x,f_y) &= \Im\{h_1(x,y)\} \\ H_2(f_x,f_y) &= \Im\{h_2(x,y)\} \end{aligned} \tag{2-9}$$

Then, a numerical "interference" between two speckle patterns is performed on the spectral domain,

$$F(f_x, f_y) = \frac{H_1(f_x, f_y)H_2^*(f_x, f_y)}{\left|H_1(f_x, f_y)H_2(f_x, f_y)\right|} = \exp\{j[\phi_1(f_x, f_y) - \phi_2(f_x, f_y)]\} \tag{2-10}$$

where $\phi_1(f_x, f_y)$ and $\phi_2(f_x, f_y)$ are the phases of $H_1(f_x, f_y)$ and $H_2(f_x, f_y)$, respectively. It is seen that

$$\phi_1(f_x, f_y) - \phi_2(f_x, f_y) = 2\pi\,(uf_x + vf_y) \tag{2-11}$$

Finally, the halo function is obtained by the second-step FFT,

$$G(\xi, \eta) = \Im\{F(f_x, f_y)\} = \overline{G}(\xi - u, \eta - v) \tag{2-12}$$

which is an expanded impulse function located at ($u$, $v$). By detecting the crest of this impulse function, the displacement vector represented by the cluster of speckles within the subimage is uniquely determined.

## 2.3 Electron Speckle Photography (ESP)

Sensitivity of speckle techniques depends on the speckle size. Use of light in visible spectrum will be sufficient for most of the applications in macro domain. Laws of physics dictate that smallest observable object cannot be smaller than the wavelength of the radiation that is used to form its image. Through use of visible light one can see speckles about 0.5μm in size. In order to use speckle metrology beyond this limit, one needs to use smaller wavelengths. One option to do is the use of electron microscope. Particles with sizes only small fractions of a micron are not visible through optical microscope, but they are easily observable under an electron microscope. With the use of electron microscope sensitivity of the technique is increased by several orders of magnitude.

There are several microscopy techniques (SEM, TEM, STEM, AFM, etc...) available. Among them scanning electron microscope (SEM) is the most suitable for testing of solid materials. For example when compared with transmission electron microscope (TEM) it does not need any complicated specimen preparation and also there is no need to use specimens with only a few micron thicknesses. Its secondary electron detector is able to acquire fine topographic images with good contrast levels and with its backscattering detector mode it can show materials with different atomic masses using different contrast levels which is very useful when using speckles since specimen and speckles are seldom same material. It has a large chamber that can hold a loading device and it allows in-situ testing. For most commercial instruments, the resolution can reach 2nm to 5nm and for advanced research ones, it can be smaller than 1nm. Large depth of field which is usually 100-500 times greater than an optical microscope makes it possible to use stereo techniques to examine rough surfaces and measure out-of-plane deformation. Another feature of SEM is that the topographic, crystallographic and compositional information can be obtained rapidly and efficiently. Finally, with the environmental function of SEM, nonconductive material can be examined without any metallic coating. The ESP technique is a combination of electron microscopy and digital speckle method. The procedure for ESP is first creating micro/nano-speckles that are used as gaging devices on the surface of the specimen to map the full field deformation. Second, recording and digitizing speckle patterns using scanning electron microscope. And analyzing speckle images by CASI (Computer Aided Speckle Interferometry) in a point-wise manner to determine the whole displacement field. The strain field is then obtained by differentiating the displacement field.

ESP extends the speckle technique to the micro/nano mechanics domain. Using random tiny particles generated by vacuum vapor deposition, ESP is able to map whole-field deformation at the micron scale with high sensitivity. The procedure for creating micro/nano-speckles will be discussed in following chapter.

# Chapter Three:

# Application of ESP to

# Experimental Study of Crack Propagation

# Characteristics in Lamellar TiAl

## 3.1 Testing System

Our testing system consists of Hitachi SEM of model S-2460N and a special loading device that can perform uniaxial tension and compression inside the chamber of the SEM. The main body of the loading device is bronze. Two screw gears connect two ends of the loading device. This loading device has enough stiffness to sustain a load up to 1000 pound. The worm gear system of this loading device has large reductions of 600:1. The large reduction of the worm gear system guarantees that the displacement

between two ends of the loading device changes on the order of nanometers. This feature of the loading device makes it possible to test specimens with dimension of microns but when testing large size specimen, the loading process would be very slow. To speed up the loading process, the worm is connected to an electric motor whose speed can be controlled.

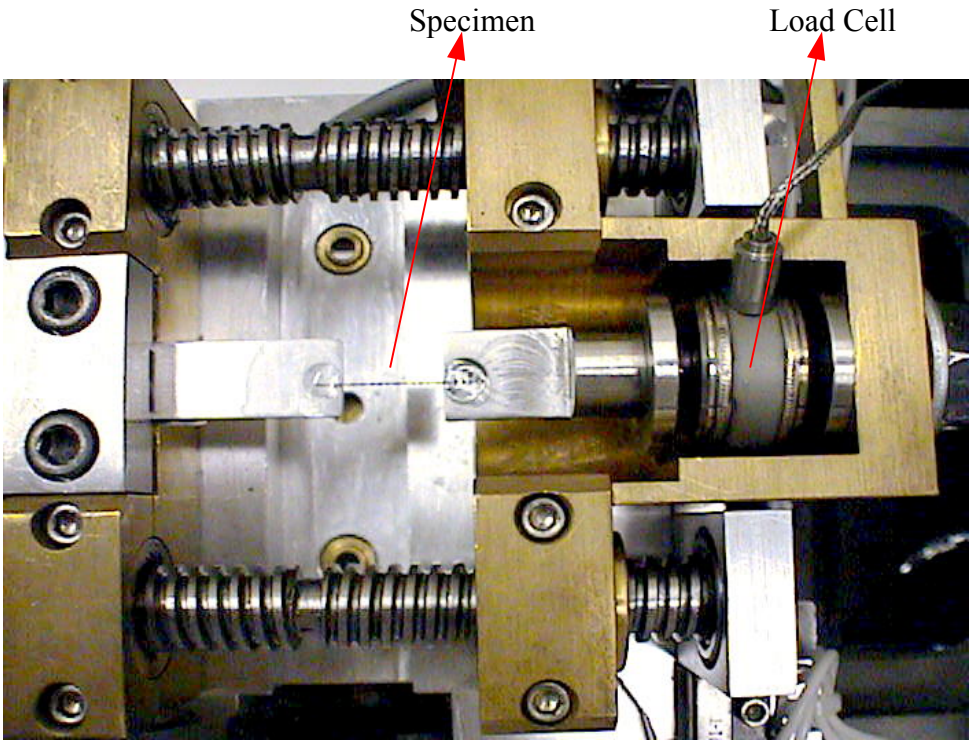


Figure 3.1 The Uniaxial Tensile Loading Device

Another issue in this loading device is the selection of the load cell. To test different size specimens, one must choose different load cells to ensure the most accurate load readings. This loading device presently has four load cells; 5 gram load cell, 50 gram load cell, 500 gram load cell and 1000 pound load cell. The number associated with each load cell indicates the full loading range of the corresponding load cell. The accuracy of each load cell is 0.01 gram, 0.1 gram, 1 gram and 0.1 pound, respectively.

## 3.2 Materials and Specimen Preparation

The composition of lamellar TiAl which determined by EDAX energy dispersive spectroscopy system was Ti-56Al with the average grain size of 450μm. Fig3.2 shows the grain structure and lamellar structure. Young's modulus of TiAl is different in different crystallographic orientations. Its modulus is about 160 GPa in [001] direction, about 130 Gpa in [010] and [-110] directions and its modulus decrease about %25 when temperature is 800°C (Zupan and Hemker, 2001).

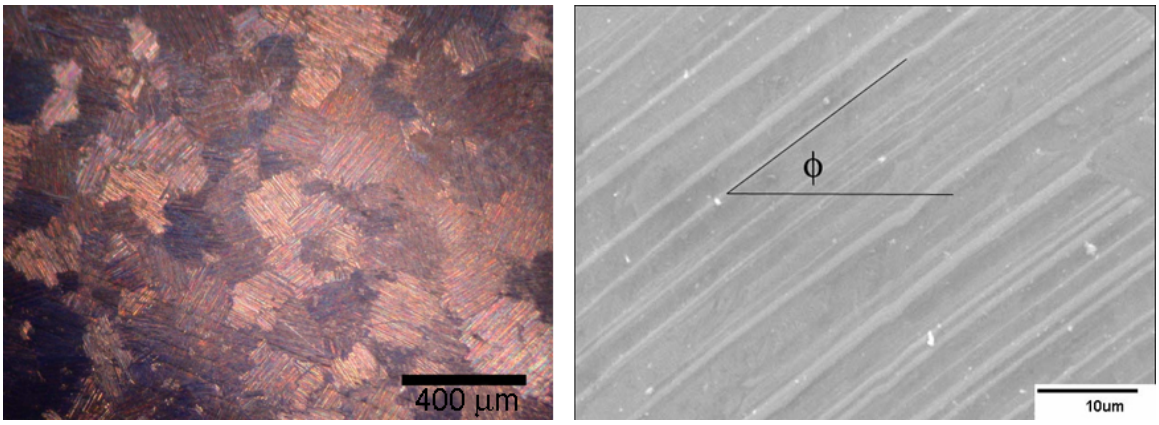


Figure 3.2 Optical & SEM Micrographs of Polycrystalline Lamellar TiAl.

Two types of specimens manufactured one is Single edge notch (SEN) coupon specimen the other type is cracked Brazilian disc (CBD) specimens. Both SEN crack and CDB of about 1mm in thickness and 3.5mm to 9mm in diameter are manufactured from the same lamellar TiAl. In SEN specimen notch cut by a diamond tipped saw which about 2 mm in thickness and specimen put under a cyclic load until a sharp crack created. In CDB specimens we were not able to create sharp cracks using cyclic loading. Notches in the middle of the disk specimens with 0.15 mm in thickness cut by Electrical Discharge Machining (EDM) and no cyclic load applied. To be able to see the grains and

lamellar structure in more detail, specimens mechanically polished by 0.05μm alumina particles and chemically etched using nitric acid. Uniaxial tension and Brazilian tests made in the special loading stage, which is capable of applying both tension and compression in chamber of Hitachi S2460N electron microscope. Test performed in constant strain rate and at a vacuum 7x10-4Pa.

SEM particles are particles or dots or any natural/artificial features of size of submicrometer or nanometer. This kind of fine pattern can be generated on a specimen surface by various techniques of thin film deposition such as vacuum vapor deposition, physical/chemical vapor deposition or sputtering etc… Currently physical vapor deposition is employed by ESP to generate speckles because of convenience and speed.

The formation of speckle through physical vapor deposition consists of processes of vaporization, transit and condensation. Source material (in our cases copper, gold or silver) is first heated in a vacuum environment to a high temperature such that large numbers of atoms and molecules leave the material surface. The heat of evaporation also provides the energy for escaped molecules to travel from the source to the substrate. When the evaporated molecules arrive on the substrate, they will be condensed to form a thin film. If the evaporation stops before the nuclei can grow and join to form a thin continuous film, a pattern of randomly distributed particles is obtained.

## 3.3 Experimental Study of Crack Propagation under Mode I Loading

Observation of the crack is performed under mode I global loading. Geometry of the specimens is shown in Figure 3.3. The specimens were loaded by tension inside the chamber of Hitachi S2460N scanning electron microscope. All tested specimens had a natural initial crack initiated by fatigue. Surfaces of the specimens were coated with random particles made of copper with size ranging from 0.5 μm to 5 μm. The surface of the specimen together with the speckle pattern was recorded digitally at various incremental loads. The loading was displacement controlled via two sets of screws at a rate of 4 μm/sec. The loading was stopped whenever we observed a sudden drop in load indicating that the crack has extended or when we saw a crack propagation in SEM screen. And a SEM picture of crack was recorded. The process takes about 1 minute. Then loading is resumed until fracture ensues.

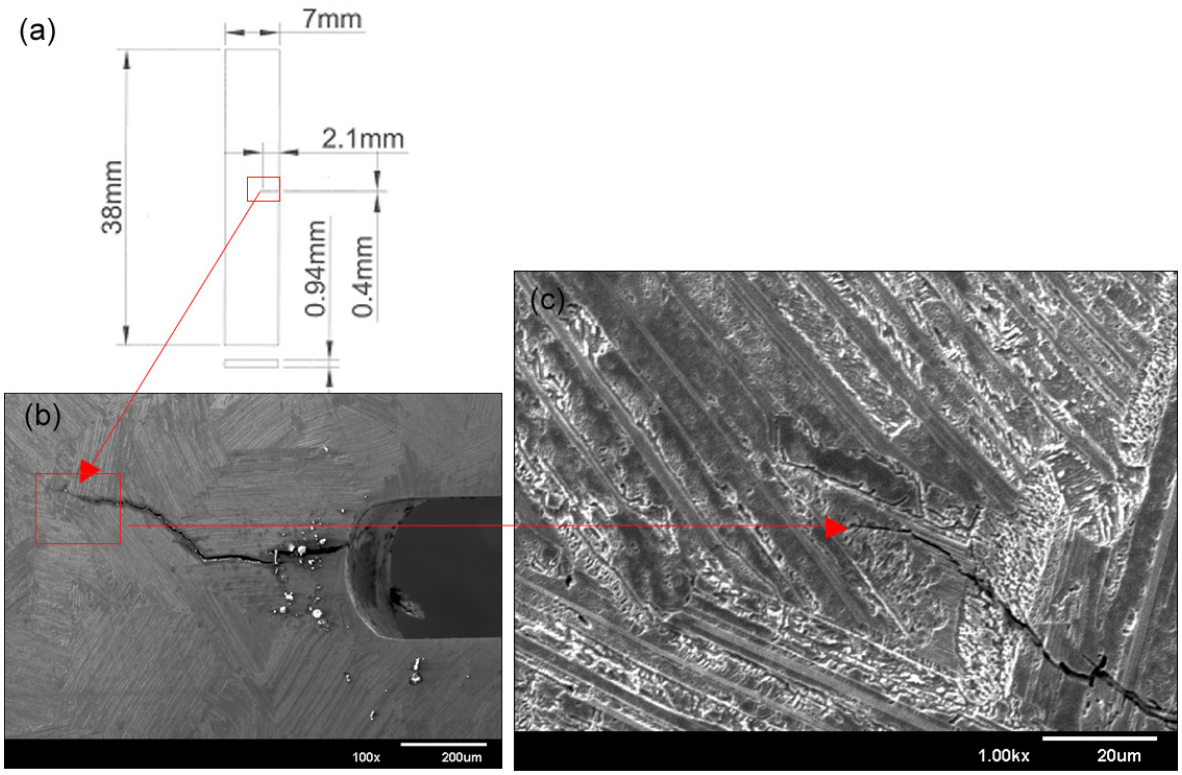


Figure 3.3 Geometry of SEN specimen, (b) initial crack generated by fatigue, (c) initial crack with larger magnification

As shown in Figure 3.3 the fatigue initiated crack from the notch has just propagated through a grain with orientation almost perpendicular to crack path. And it is arrested at the junction of many grains concentrating together (see the enlarged view).

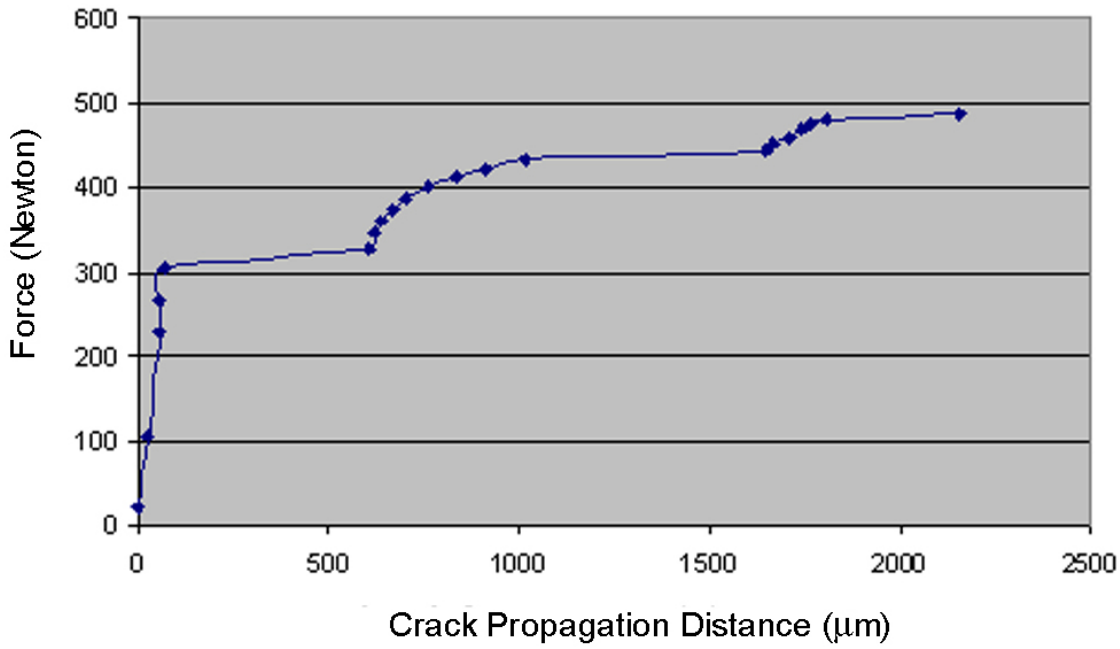


Figure 3.4 Load-extension history of a crack in a simple tension specimen with a single edge notch

The picture shown in Figure 3.3 indicates that the initial fatigue crack was arrested when it reached the junction of a cluster of grains. Figure 3.4 shows the crack extension curve. After the observation of initial crack we started to load the SEN specimen under uniaxial tension. We were unable to capture the propagation of the initial crack until 22.2 N. As shown in Figure 3.5, tip of the main crack came to a grain whose direction is perpendicular to crack path. The initial slope of crack-extension curve between 22.2 and 105.8 N implies that there is considerable resistance for the crack advance. Indeed the pictures in Figure 3.5 at loads of 22.2 (red dot) and 105.8 N. (green dot) shows that crack tip did not moved in to the next grain..

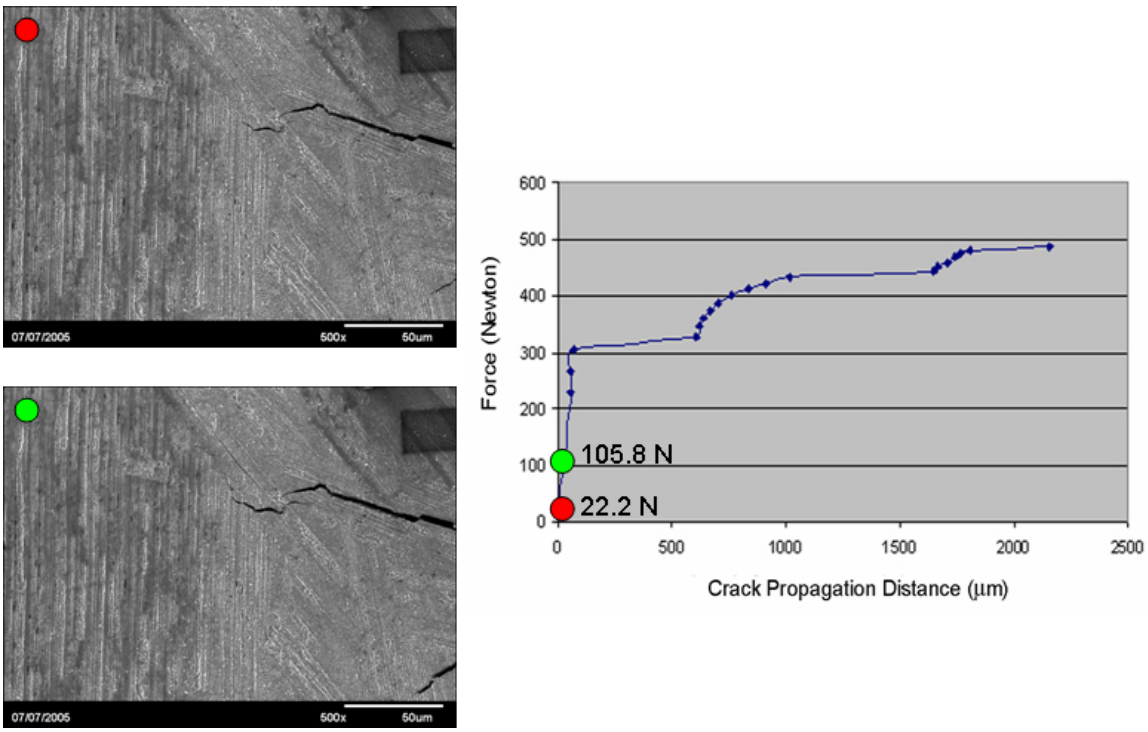


Figure 3.5 Crack extension as a function of load and the crack tip position ant 22.2N.

While the main crack did not extend much, for this load another crack had started to appear below the main crack. As the load was further increased, both the main and the secondary crack extended simultaneously but at different rates, until the load reached 304.2 N. As shown in Figure 3.6, an additional load to 326.9 N caused the crack to jump across a grain boundary. During the loads between 304.2 and 326.9 N crack tip did not move and both faces of the crack opened. After jumping in and propagating through to the next grain with almost parallel direction and without resistance, the crack tip again was arrested in the middle of a cluster of grains. Considerable resistance to further crack extension was again evident when the load was increased from 326.9 N to 433.7. as shown in Figure 3.7. During

this period crack tip tries to align itself with the grain orientation. It is more evident in high magnification pictures as shown in Figure 3.9.

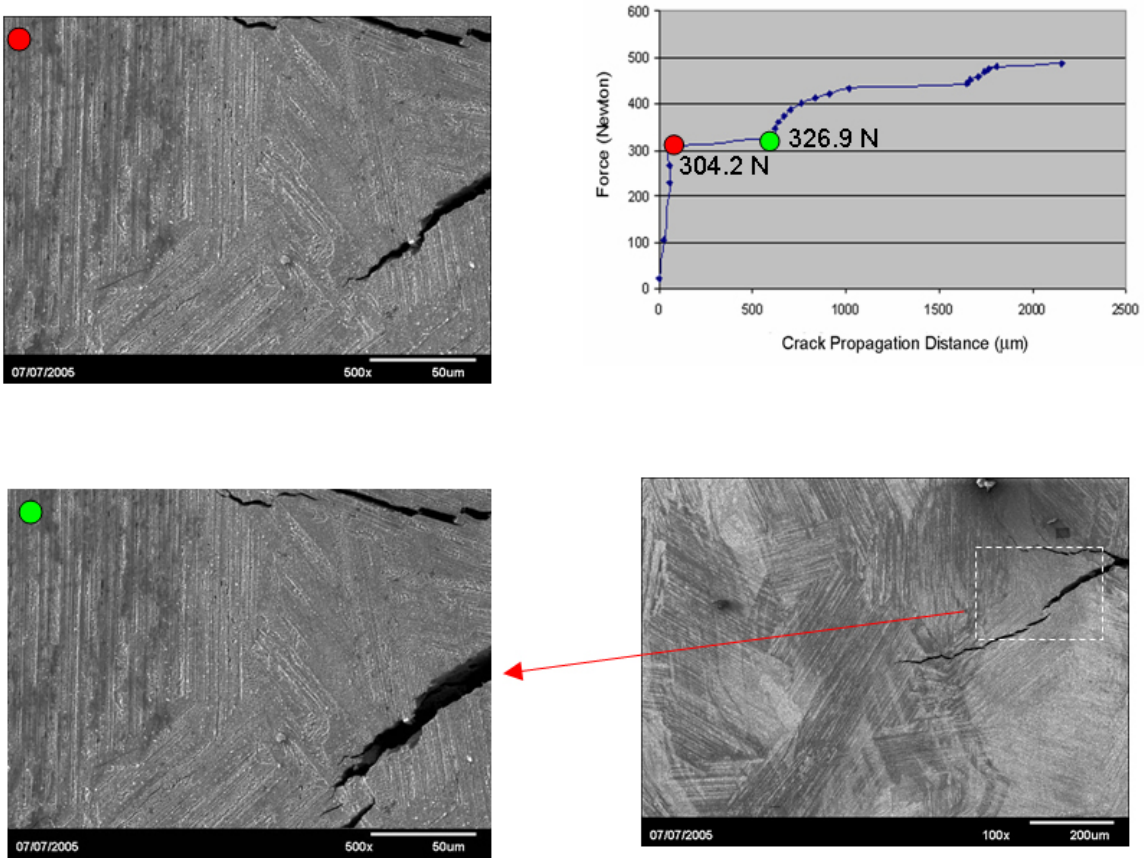


Figure 3.6 The secondary crack jumped across grain boundary.

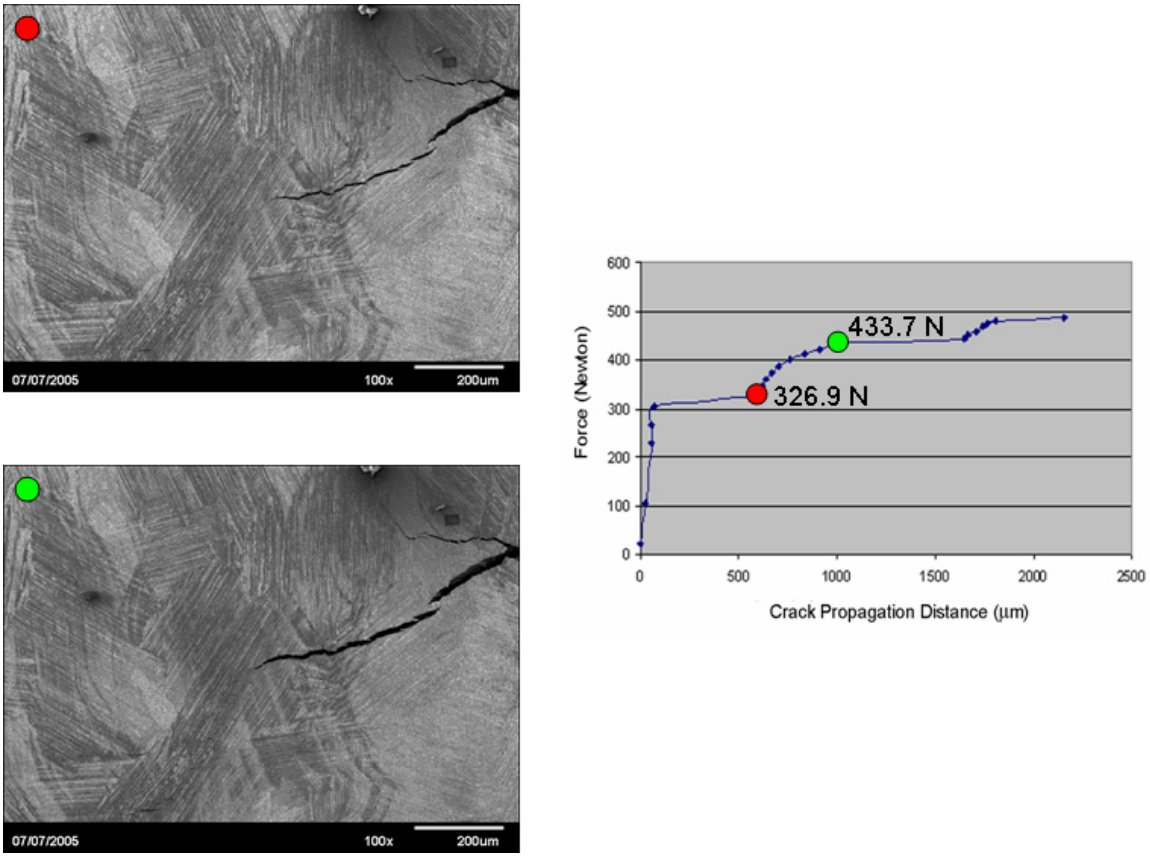


Figure 3.7 Slow crack growth period between P = 326.9 and P = 433.7 N

Another slow growth period as shown in Figure 3.8 where it is seen that between the loads 459 N and 480.8 the crack was laboring thorough a cluster of grains with various orientations. Further increase of the load resulted in unstable crack propagation which was not observable in SEM.

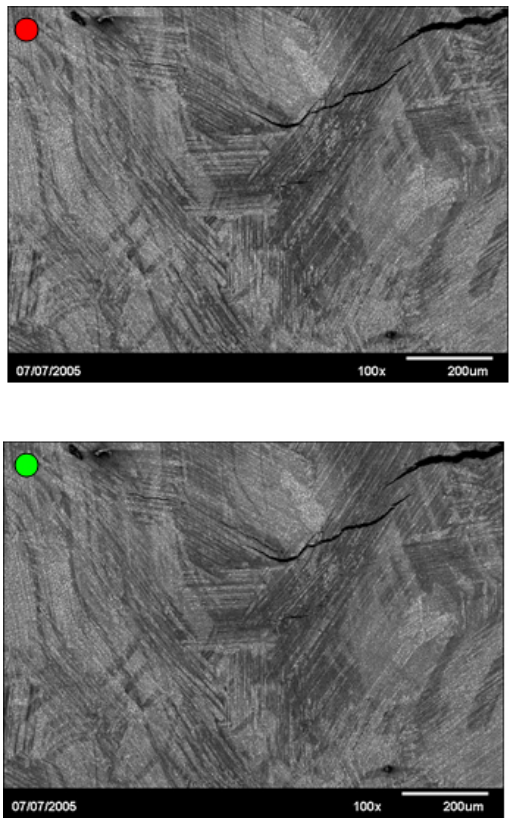


Figure 3.8 Slow Crack Growth Period between P = 450.6 N and P = 480.8

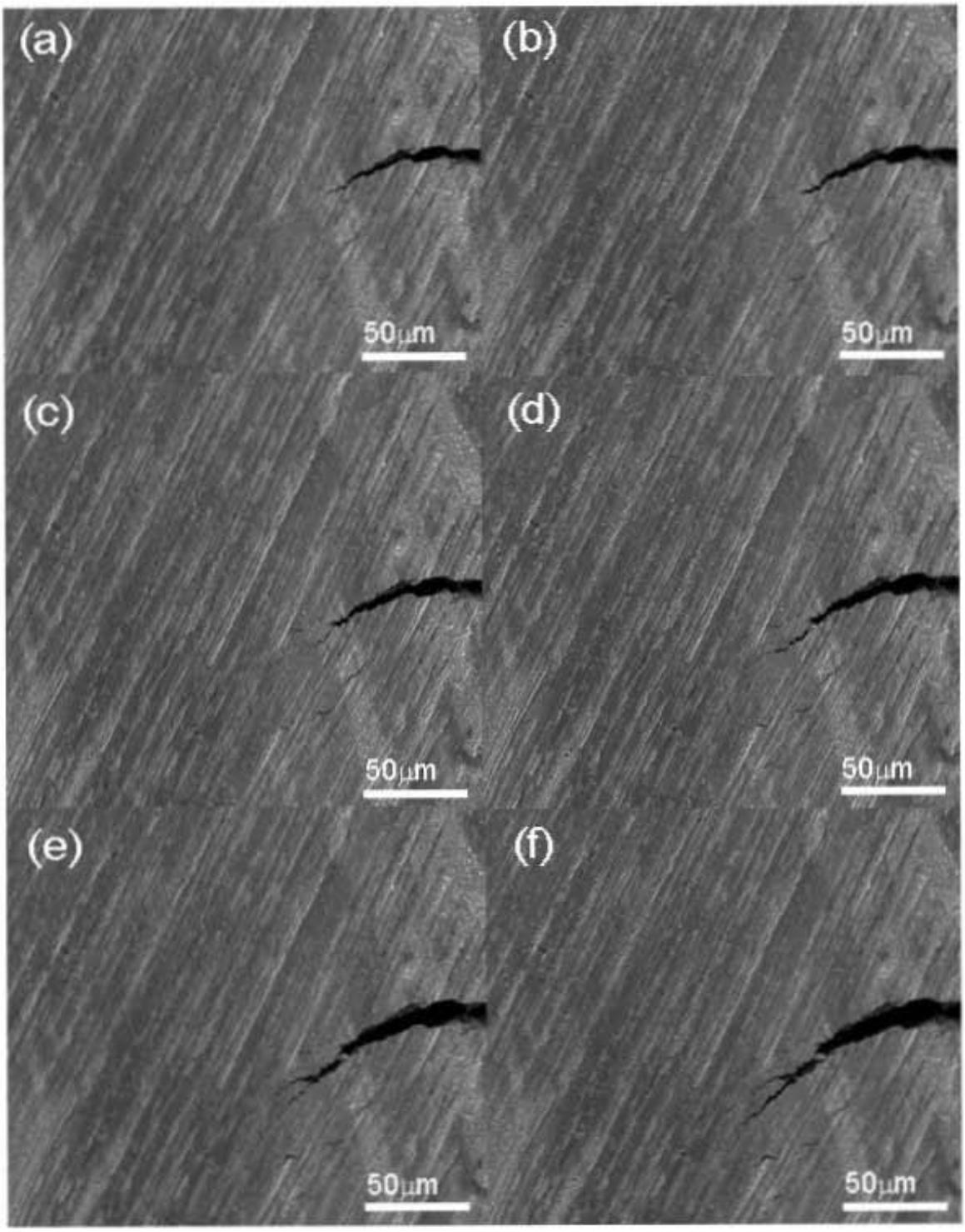


Figure 3.9 Slow crack growth period between P = 326.9 N and P = 433.7 N. Crack tip tries to align itself with the grain orientation.

## 3.4 Experimental Study of Crack Propagation under Mixed Mode Loading

Cracked Brazilian Disk (CBD) specimens were manufactured from the lamellar TiAl. Geometry of the specimens is shown in Figure 3.10

| □□□□□□□□□ | | □ | □ | □ | □ | □ | □ | H** | K** | □ |
|---|---|---|---|---|---|---|---|---|---|---|
| □□□ | □ | □ | □̃□ | □̃□ | □ | □ | □ | 7 | 9 | □ |
| □□□ | ̃ı□□ | ̃ı□□ | ̃ı□□ | ̃ı□□ | ̃ı□□ | ̃ı□□ | ̃ı□□ | 1.45 | 1.45 | ̃ı□□ |
| 2a/D | ̃ı□ | ̃ı□ | ̃□ | ̃□ | ̃□ | ̃□ | ̃□ | 0.17 | 0.2 | ̃ı□ |
| β | ı□□□ | ı□□□ | ̃□ | □□□ | □□□ | □□□ | □□ | □□□ | $25^o$ | $20^o$ |

..□□□□□□□□□□□□□□□□□□□□□□□□□□□□□□□□
□□□□□□□□
..□□□□□□□□□□□□□□□□□□□□□□□□□

Figure 3.10 Geometry of the cracked Brazilian disc test specimen

As shown in Figure 3.11, specimen A was loaded to 1912 N. Further loading led to failure without obtaining any additional information. Examination of the v-field displacement contour indicates the strain concentration at the tips of the central slot.

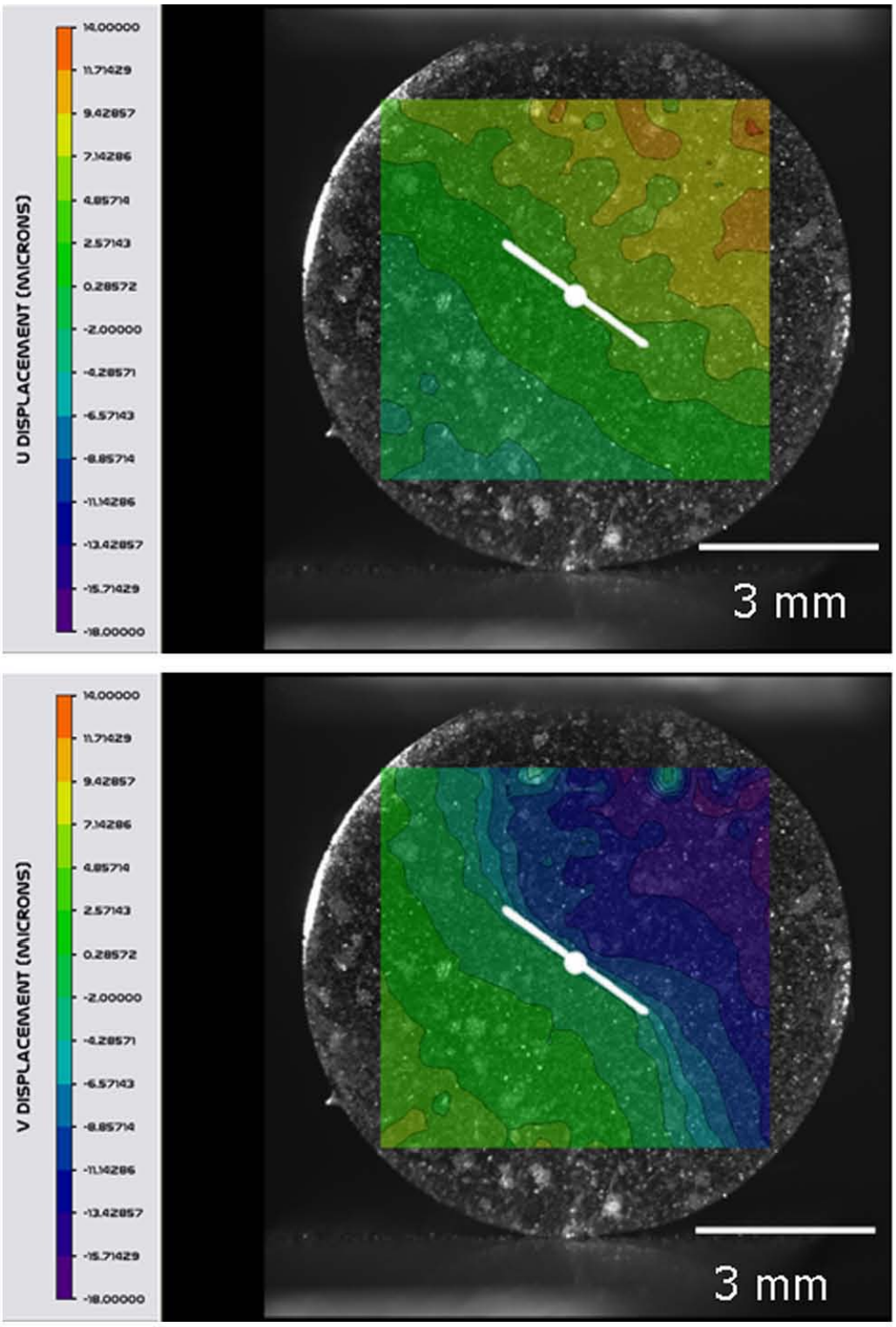


Figure 3.11 Displacement fields of a 9 mm Brazilian disk under compression prior to crack initiation.

In order to reveal more information at the crack tip, several CBD specimens were tested inside SEM and viewed at different magnifications. To control the deformation mode we used the results given in Fett. et al (2001). Specimen B ($\beta = 149^{o}$) was tested in mixed mode. Figure 3.12 shows the displacement field under a load of 1276.6 N. Examination of the v-field displacement contour reveals that the highest fringe density (thus the highest $\varepsilon_{yy}$ ) occurs at the point where the straight line edge of the slot meets the curved surface.

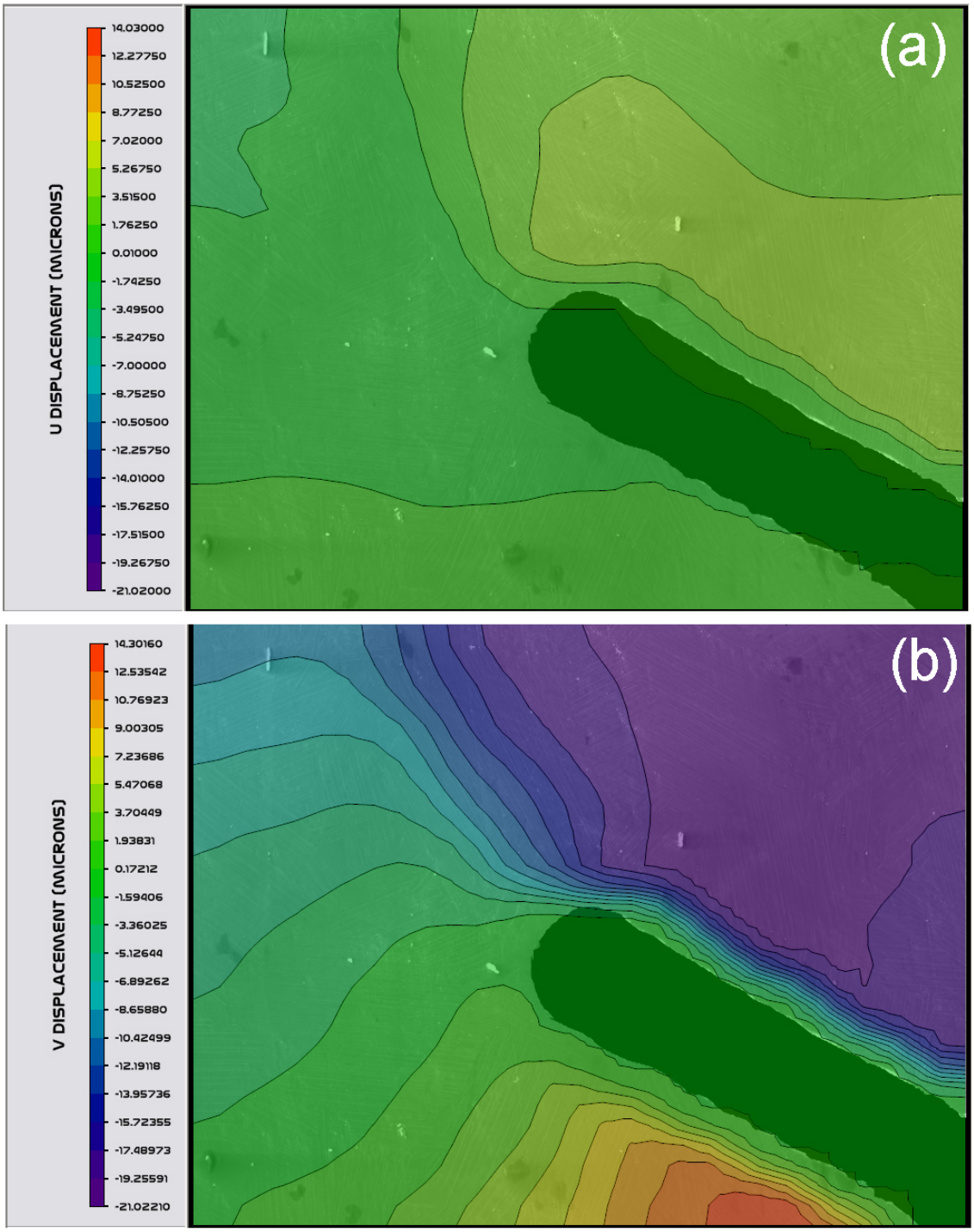


Figure 3.12 Displacement fields of specimen B prior to crack Initiation. (a) U-field

(b) V-field

An additional loading to 1290 N. result the simultaneous appearance of two cracks at the ends of the slot and load dropped to 287 lb. The locations are indeed at the points where the straight and curved edges meet as shown in Figure 3.13.

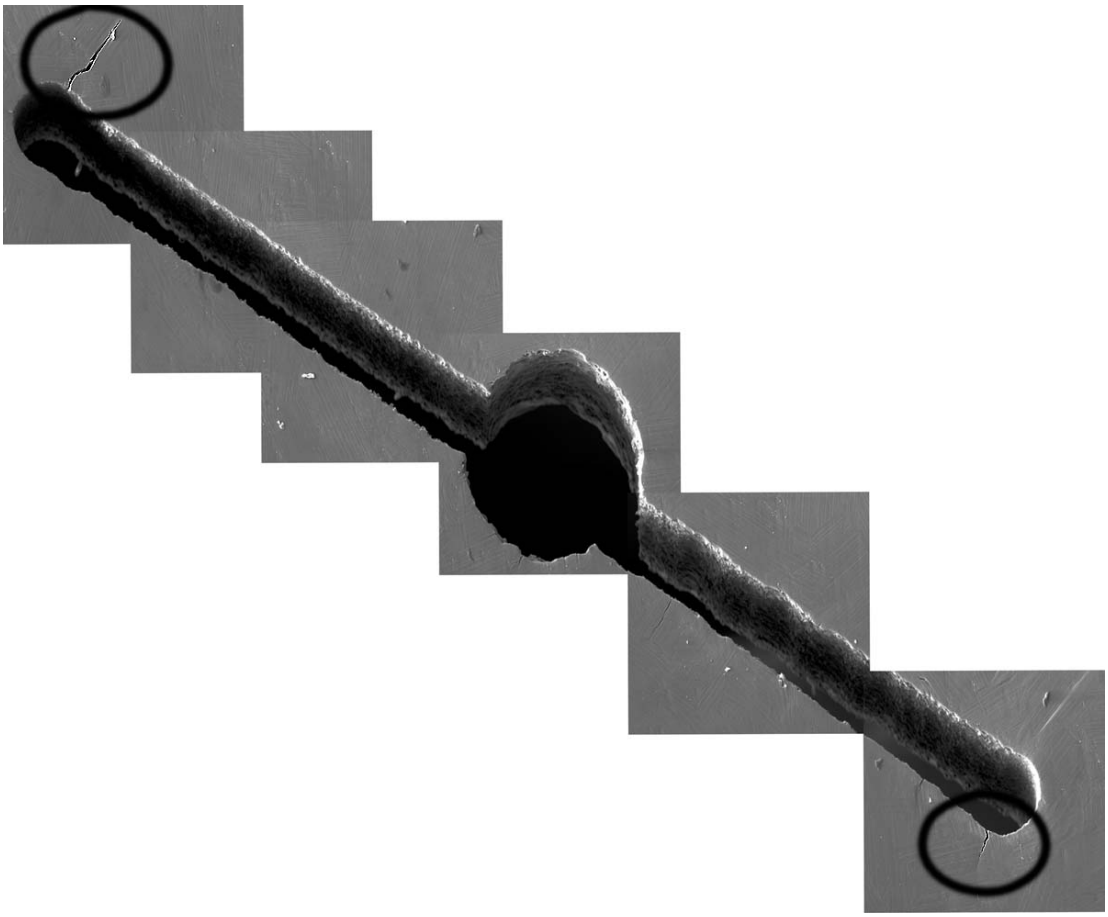

Figure 3.13 Two cracks appear at the ends of the central slot of the 7mm Brazilian disc.

Further loading of P = 287 lb to P = 291.4 lb did not advance the crack much (only a few microns). This is the region where the crack was arrested in the triple junction of grains. The displacement contours of an incremental load of P = 282.3lb to P = 288.7 lb are shown in Figure 3.14. Also shown in the figure is the crack tip position relative to the grains. Additional load caused the crack to propagate unstably and led to dynamic fracture of the specimen.

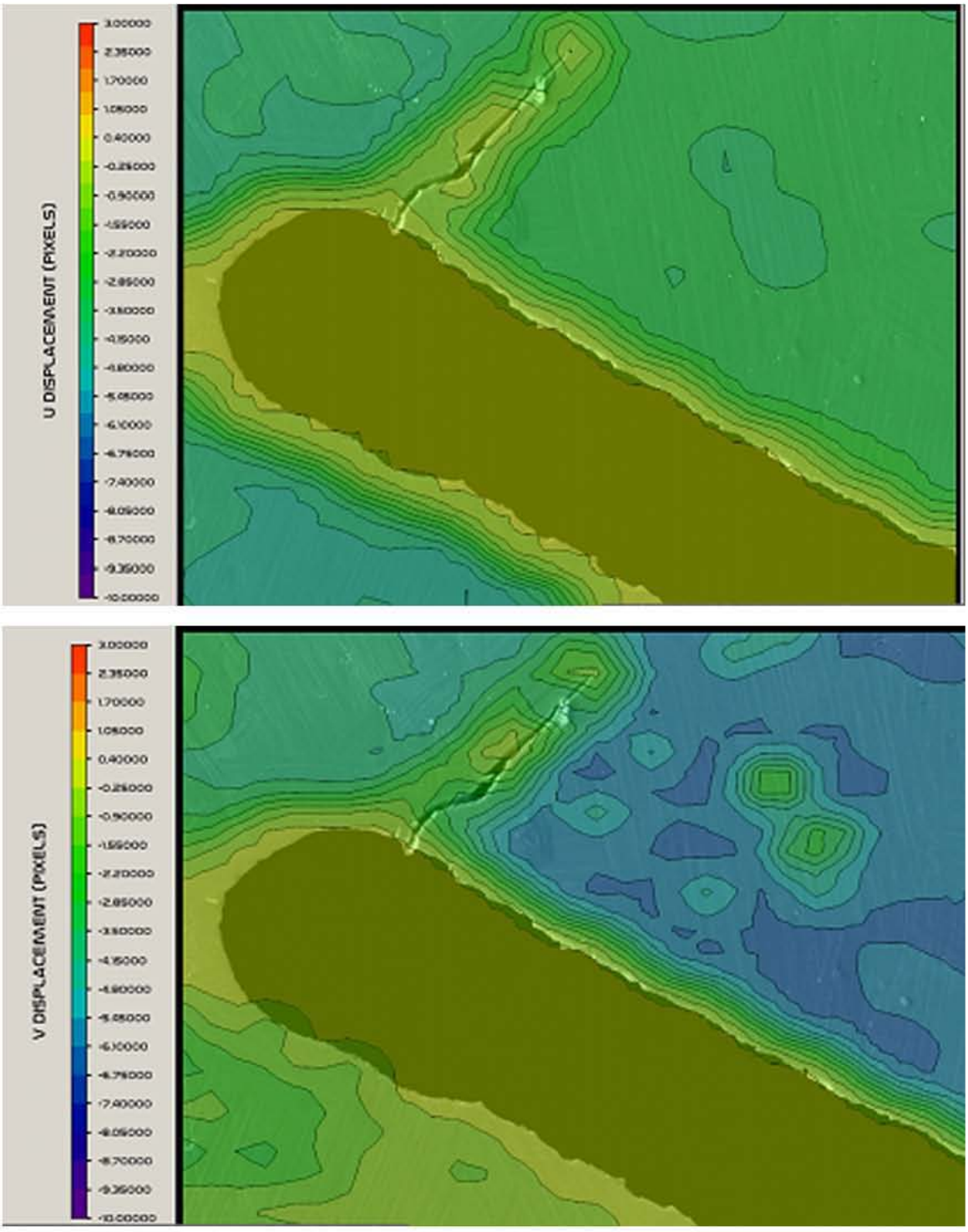


Figure 3.14 Crack tip deformation fields u (top) and v (bottom) fields.

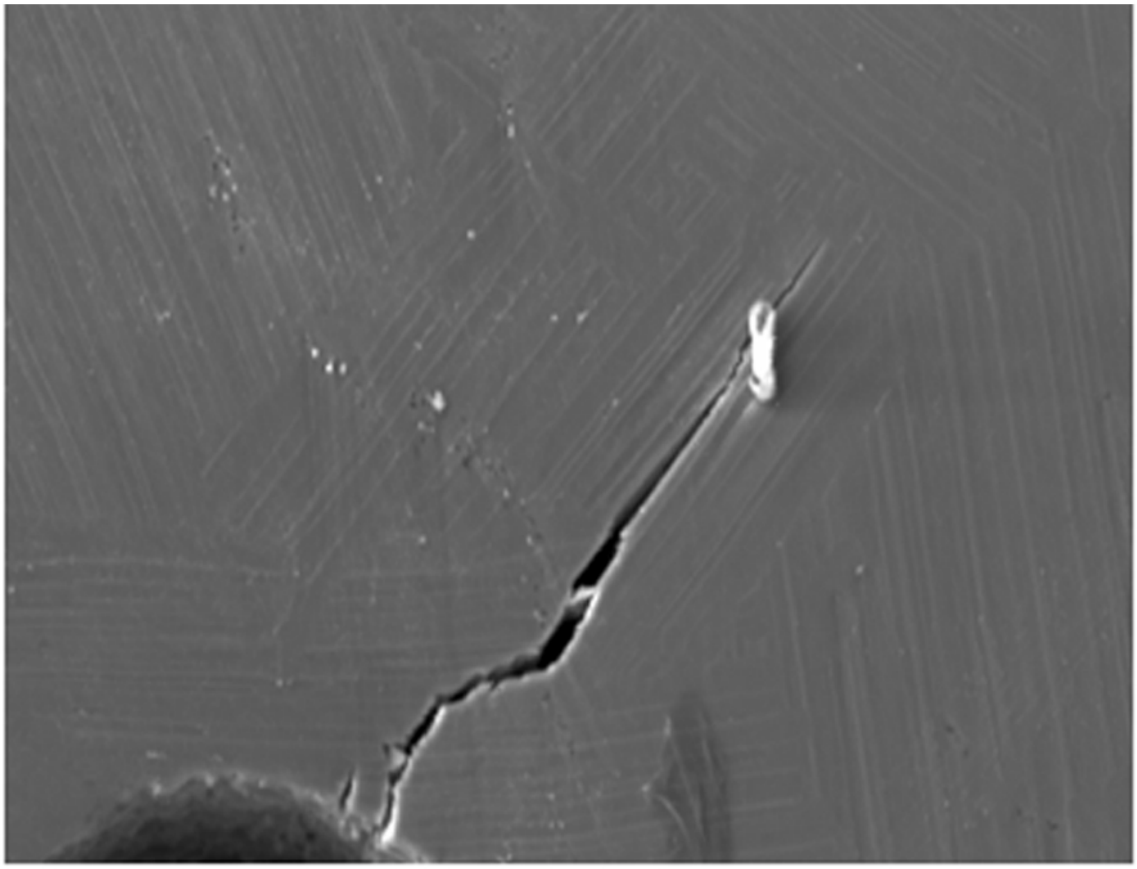

Figure 3.14 Crack tip location

Specimen C was tested in mode I ($\beta = 0^{o}$). Figure 3.15 (a) and (b) depicts the deformation pattern prior to crack initiation. Figure 3.15 (c) shows a crack initiated at the bottom tip of the central crack at P=190 lb. With further loading the crack started to propagate. At the load P= 263 lb crack tip approached to grain boundary and two cracks on bottom and above of the central crack initiated which was parallel to grain orientation. When loading continued the first crack entered a blunting process, with larger crack opening displacement as the load increased.

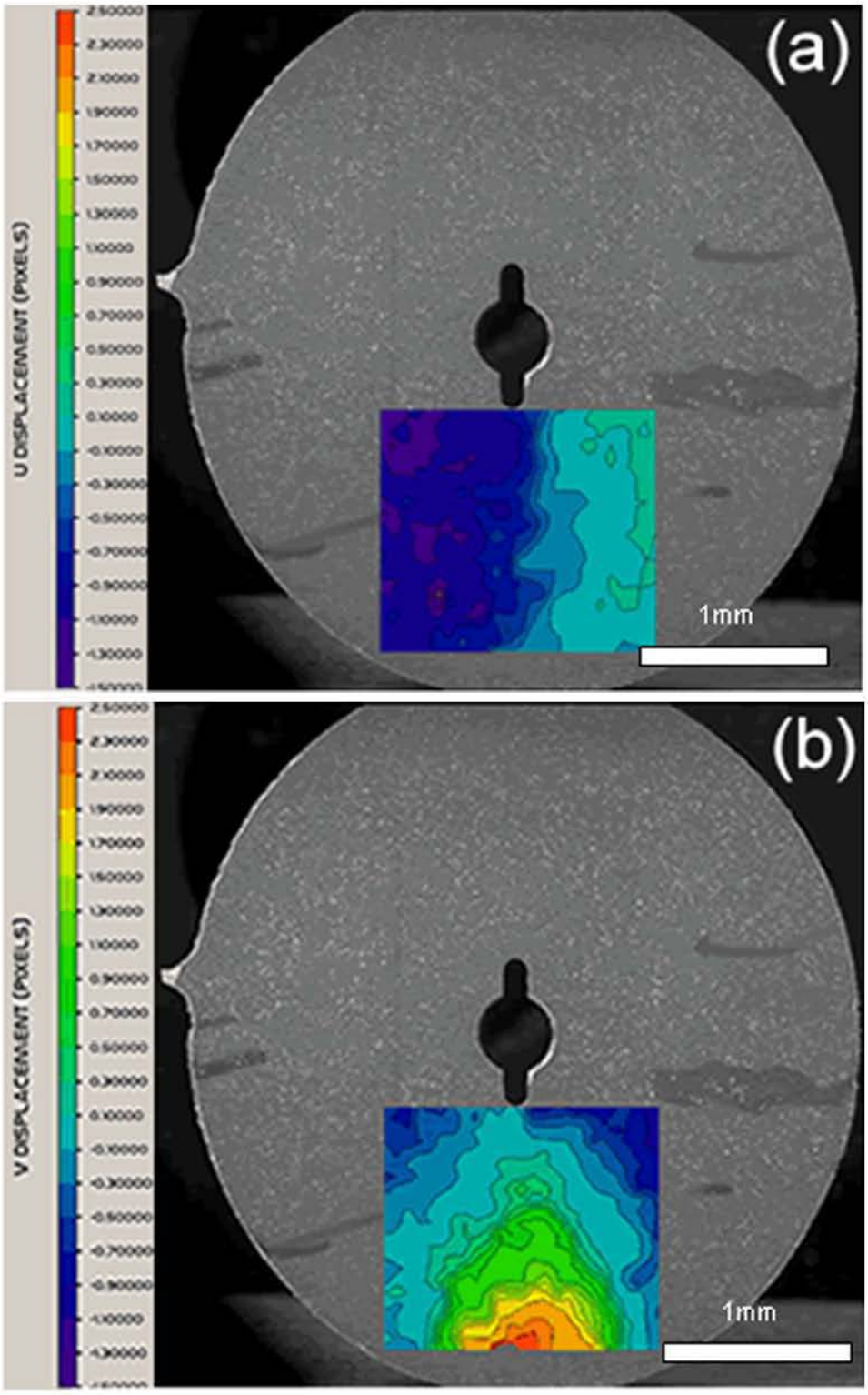


Figure 3.15 Displacement fields of specimen C prior to crack initiation. (a) U-field (b) V-field.

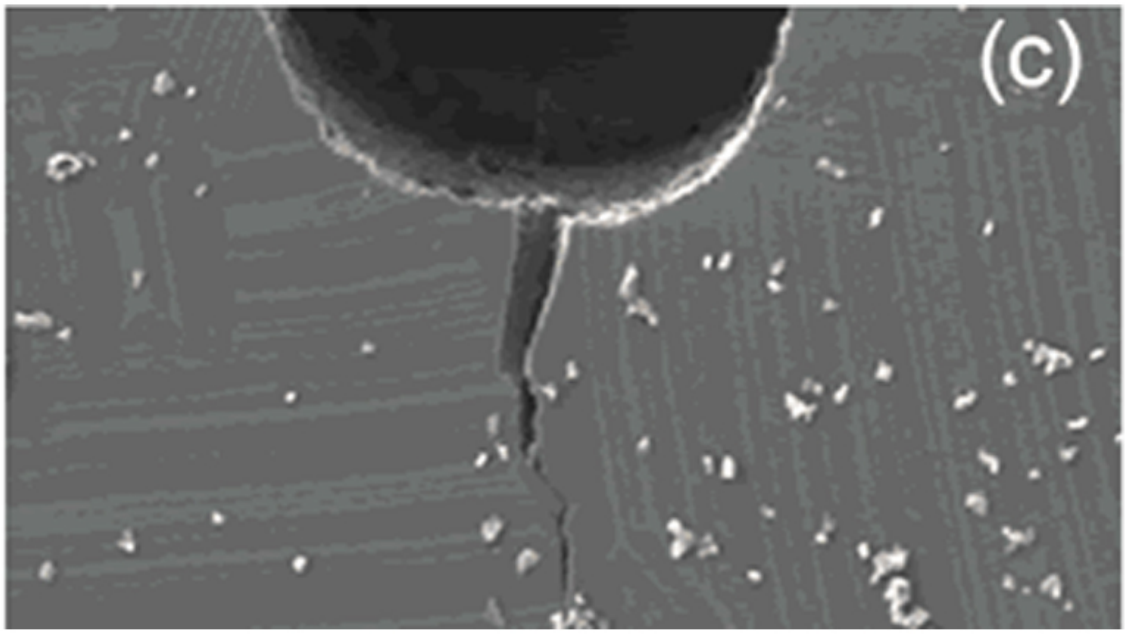


Figure 3.15 (c) crack after Initiation.

As illustrated in Figure 3.16 as second crack on the bottom started to link itself with the first crack. After the two cracks met in the same grain and they linked themselves with a ligament. Further loading to P=344 lb broke the disk into two pieces

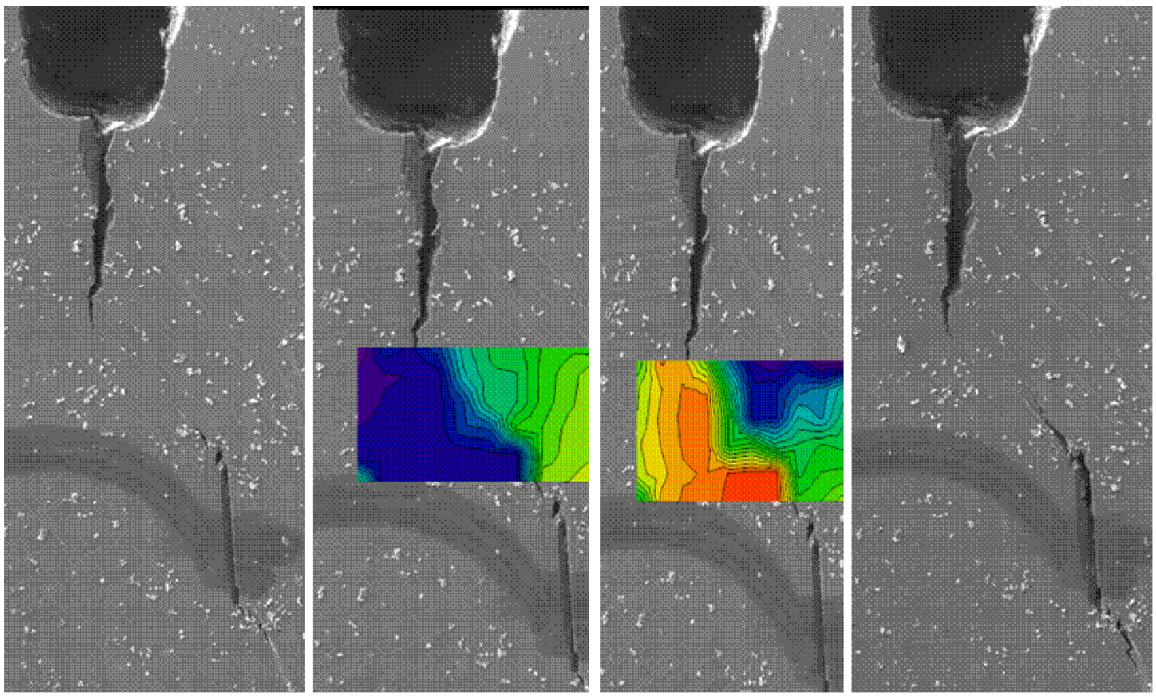

Figure 3.16 Linkage between two cracks via mode II.

Specimen D was tested with β =32° as shown in Figure 3.17. Cracks above and below the central crack were initiated at P=166 lb and P=183 lb respectively. The upper semi crack approached to a grain boundary whose orientation was nearly perpendicular to crack. The crack was arrested in that region and blunting process started. With further loading another crack was initiated near the upper crack in the same direction with the grain. Lower semi crack did not met to a grain with normal orientation. Thus it continued to propagate as further loading was applied and the failure occurred.

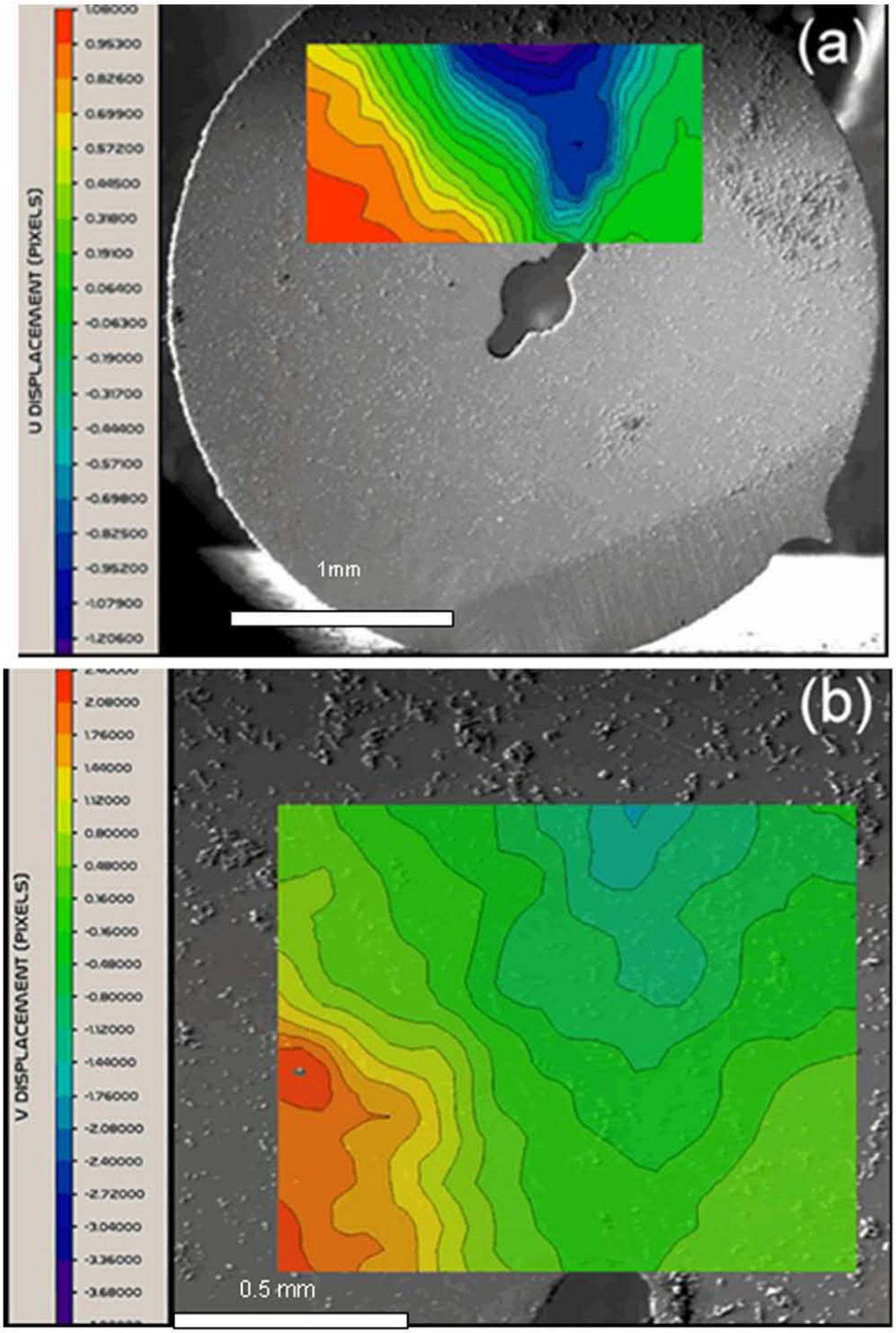


Figure 3.17 u and v fields prior to crack initiation, (a) u field at 25x, (b) v field at 100x

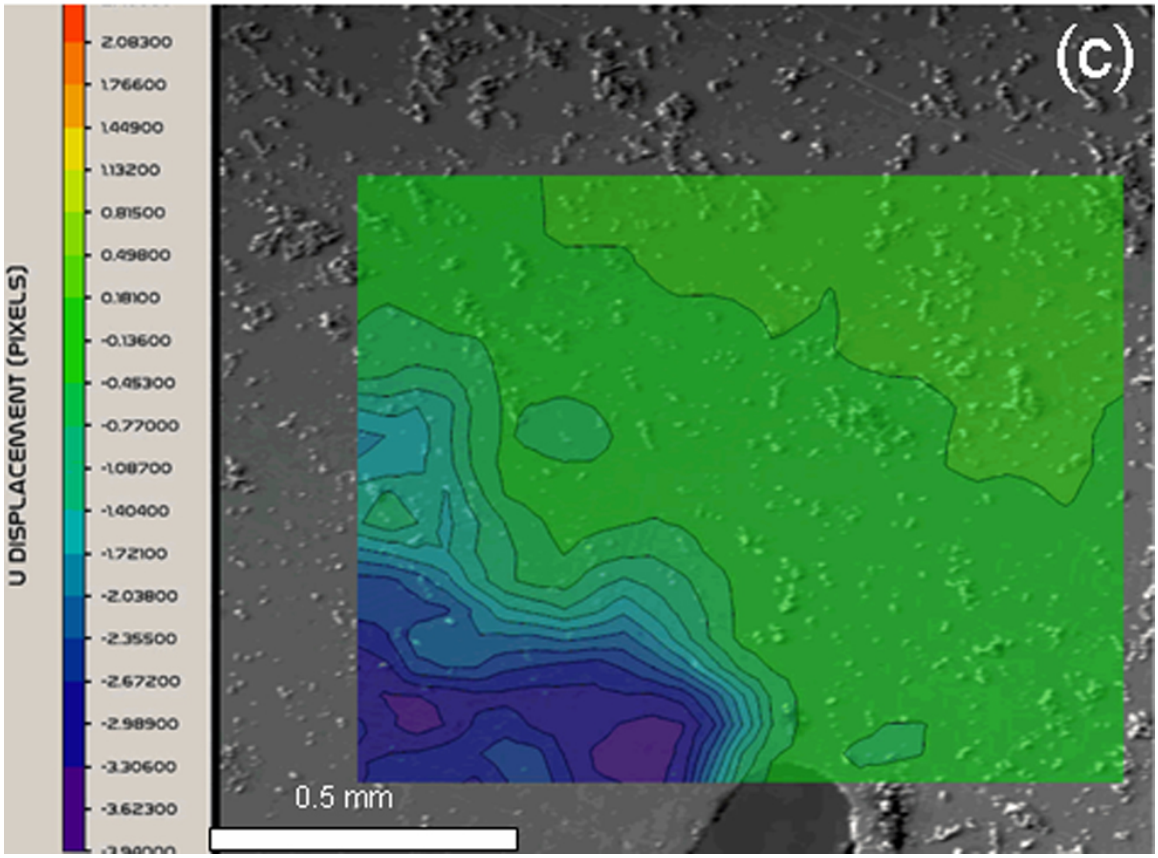


Figure 3.17 u and v fields prior to crack initiation (c) u field at 100x in specimen D.

During the tests we observed microcracks in front of the main crack tips. These microcracks were initiated with the orientation almost parallel to the loading direction and they propagated through the grain by extending the crack length in both directions.

## 3.5 Discussion and Conclusions

During the early stages of uniaxial tests we found that the ε-σ curve has a zigzagging behavior, we believe this non linear response is largely due to the re-arranging of the grains as the load is applied. Once the rearrangement is complete, the specimen will deform uniformly as the load further increases. For a given uniaxial tension specimen, the strain at the grain boundary can be seven times smaller than the interior of

the grain. Also the experimental results demonstrate exclusively that grain boundaries act as crack retarders. Whenever a crack enters the junction of a cluster of grains, it slows down and seeks the path of least resistance; it tends not to propagate along the direction perpendicular to the lamellar layers. When the crack tip reaches the grain boundary, the direction of its further extension can be predicted by the strain field surrounding the crack tip region. Figure 3.18 shows such an example. The shear strain field obtained by electron speckle photography technique indicates strain concentration appearing only on one side of the crack demonstrating that the strain free side is moving as a rigid body.

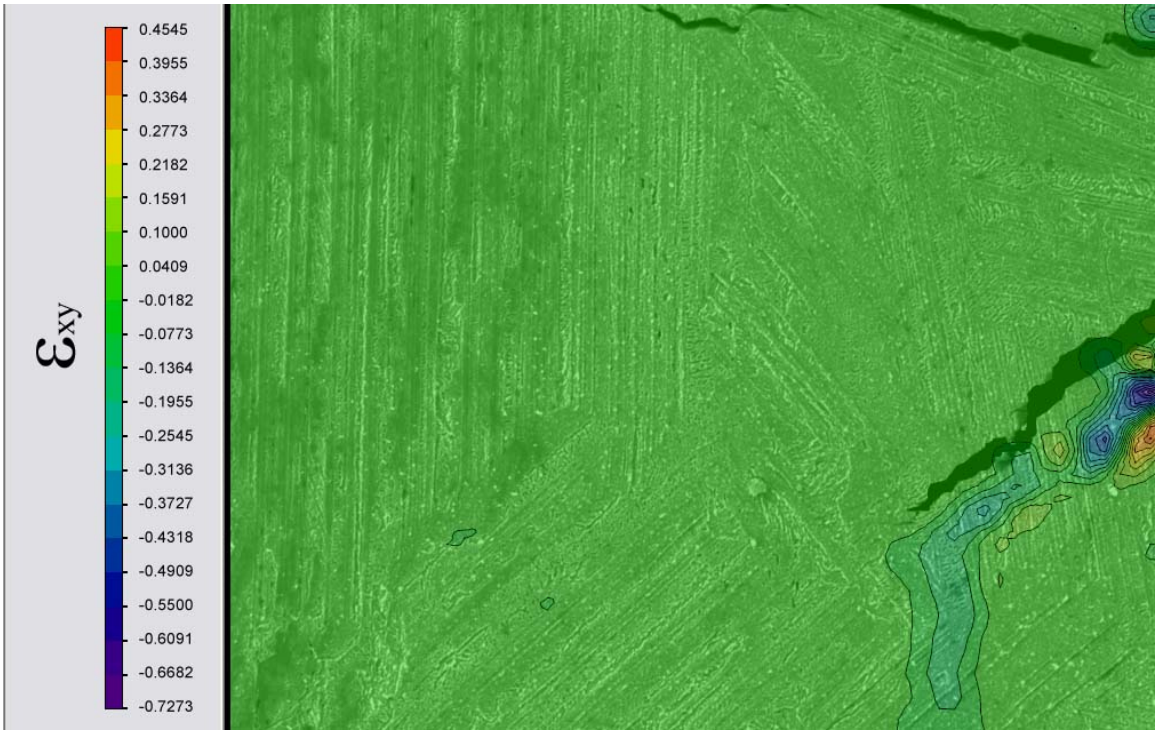


Figure 3.18 Shear strain field prior to the crack jump across grain boundary.

The shear strain extents into a region where is no observable crack. Figure 3.19 depicts the superimposition of shear strain field with trace of the crack tip at 326.9 N. It is clear that the direction of the crack propagation followed the shear strain concentration.

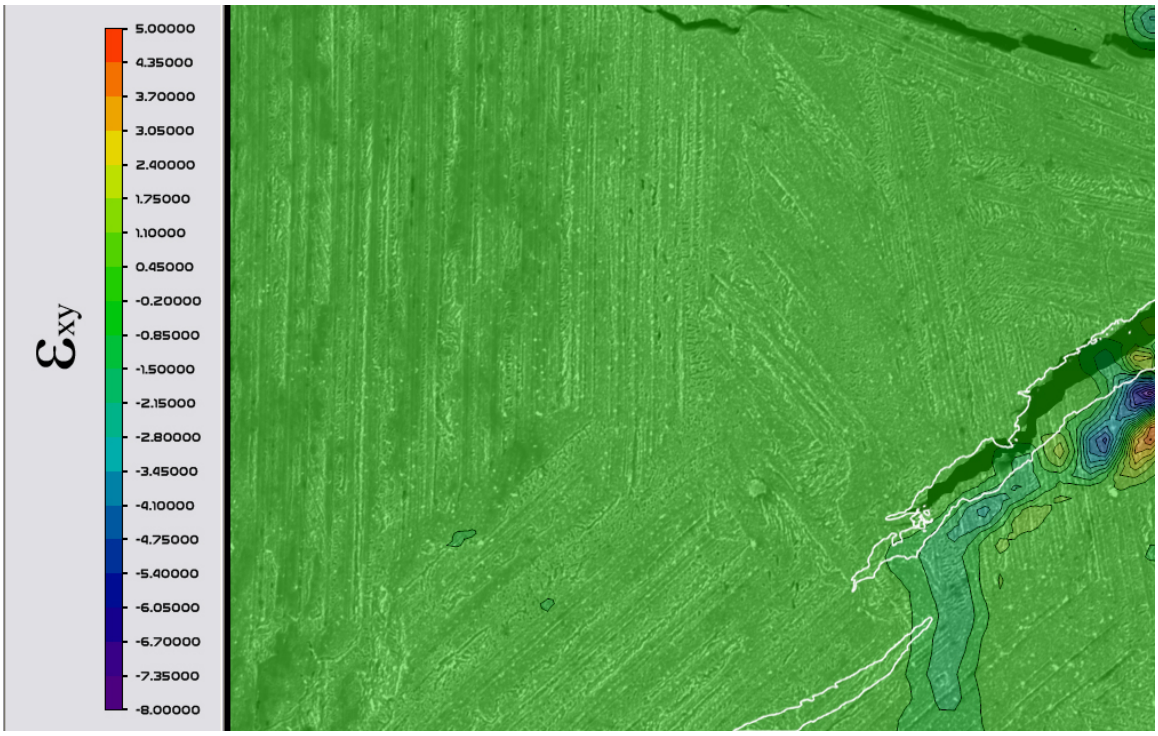


Figure 3.19 Superposition of shear stress field prior to crack jump with the trace of the jumped crack.

Another example can be given in Figure 3.20. It shows the displacement and strain fields surrounding the upper edge of the notch in specimen C prior to crack initiation. Strain field indicates the area of high strain concentration. Further loading resulted in new mode I crack initiated at a distance away from the main crack in grain with orientation similar to the loading direction. Within the area indicated by of high strain concentration.

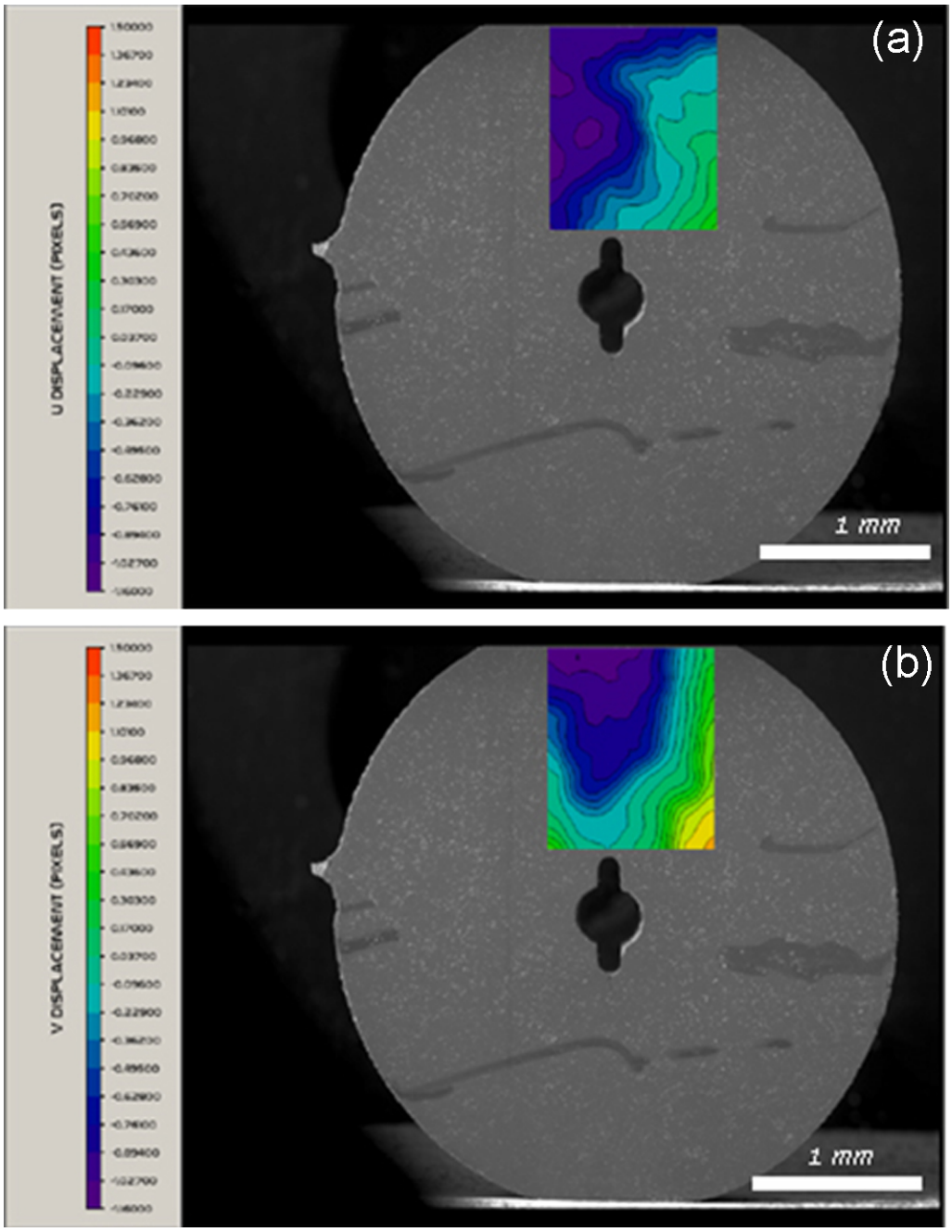


Figure 3.20 Displacement fields of specimen C prior to crack initiation. (a) u-field (b) v-field.

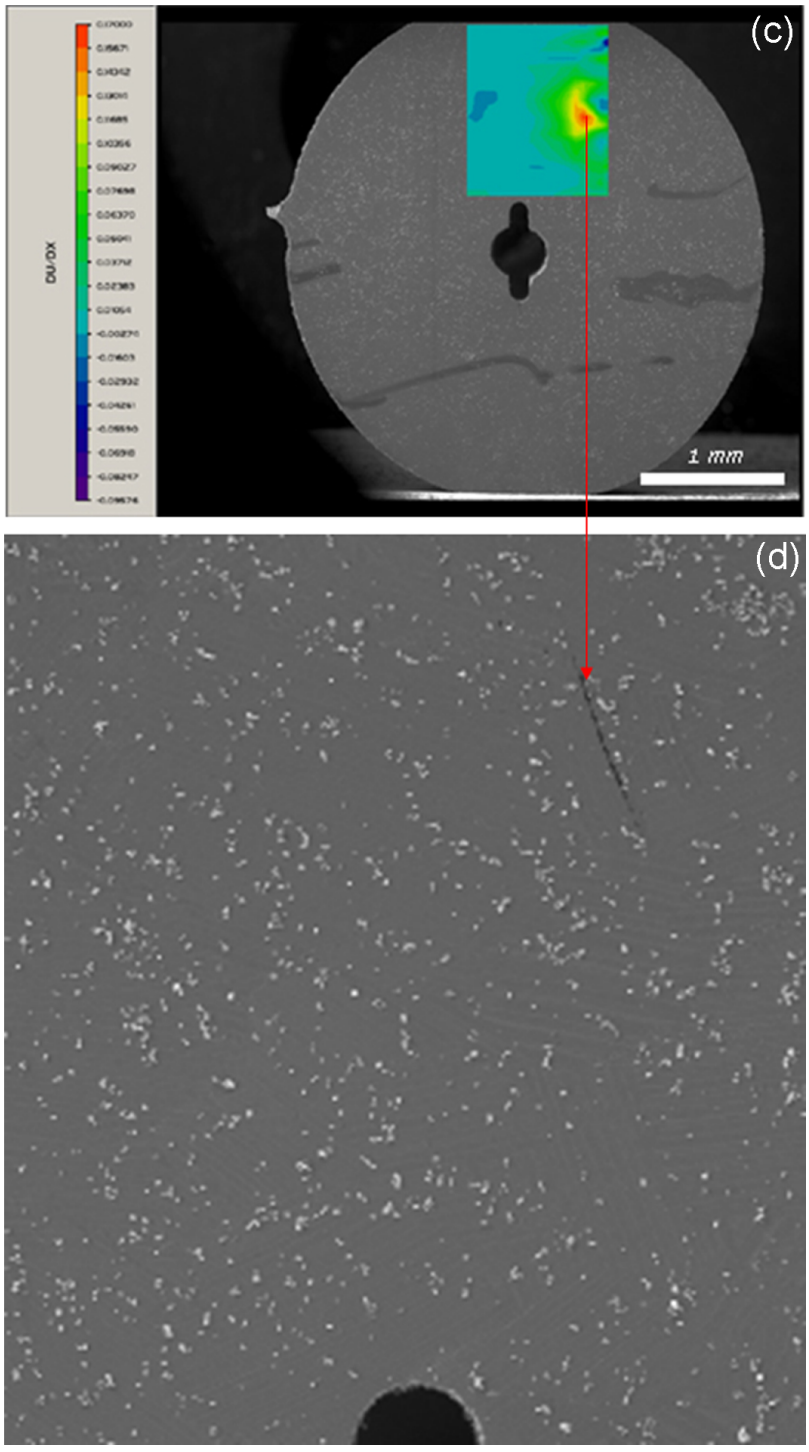


Figure 3.20 (c) $\varepsilon_{xx}$ strain field. (d) crack initiated in the site indicated by strain field (Shown by the red arrow).

During the uniaxial tension tests with SEN specimens, microcracks whose directions are perpendicular to the grain orientation initiated but they did not propagate. In the case of Figure 3.21, crack tends to change its orientation along the lamellar direction. Microcracks that are perpendicular to the lamellar orientation were created in front of the main crack. After additional load those microcracks linked themselves with the main crack and entered to the next grain without too much resistance. I t can be seen from Figure 3.21 that microcracks (arrow shown in Figure 3.21) have similar direction with the next grain on the left. These microcracks may serve as a propagation path for the main crack. In this study we were just able to see the surface features of the specimen. It could be the case that next grain on the left is reaching beneath the other grain. In Figure 3.21 strain field $\varepsilon_{xy}$ shows a clear shear band between the new and the main crack, in this case indeed shear band plays an important role in the propagation mode resulting in the sliding of layers against each other and thus linking the main crack with the new crack. Even if there is a shear band, the magnitude of $\varepsilon_{yy}$ seems to indicate that the crack faces would open as well.

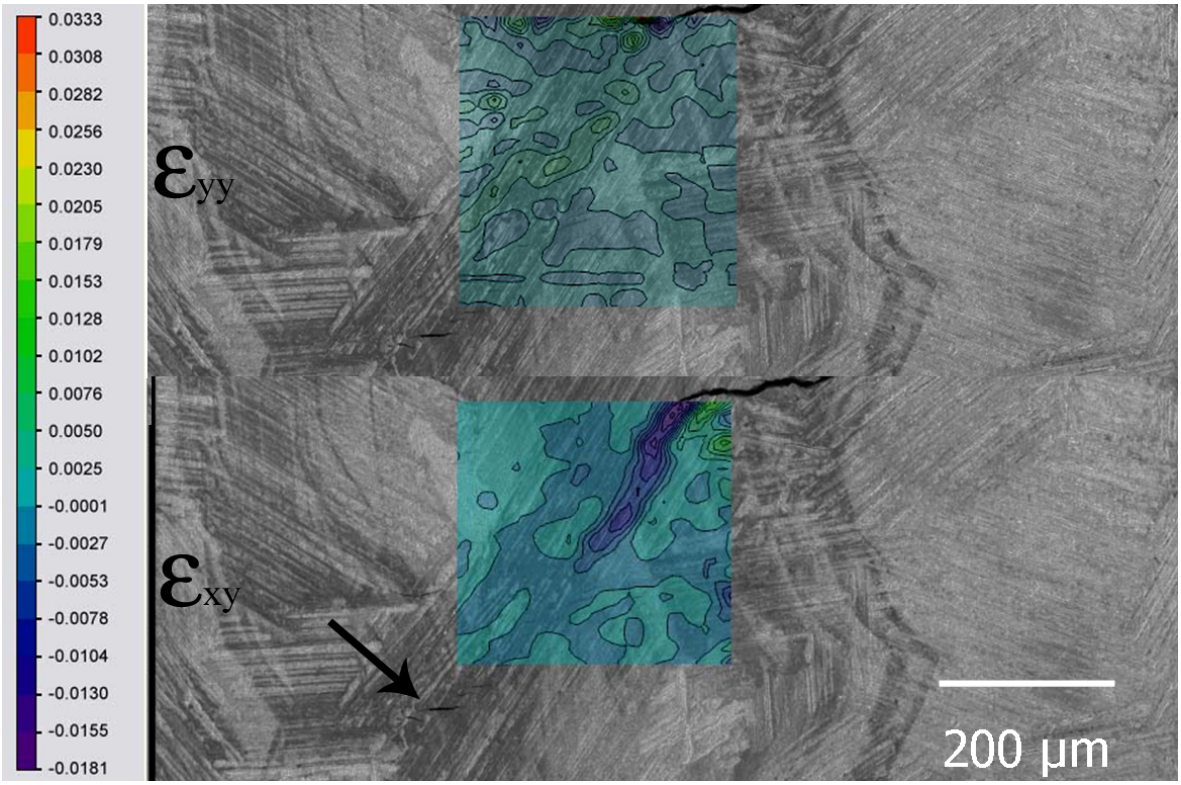


Figure 3.21 Strain field surrounding the crack tip between P= 400 N and P= 445 N.

In case of Brazilian tests we also observed microcracks in front of the crack tip as depicted in Figure 3.15 and Figure 3.16. Different from uniaxial tests, these microcracks initiated in the same direction with grains (and also loading direction) and again main crack connected itself with these microcracks by sliding two faces of the grain against each other as shown in Figure 3.21. Its worth to note that in uniaxial tests the microcracks in front of the main crack did not propagate after initiation they served as a path for main crack, but in compression tests the microcracks initiated in the same direction with the grains and they propagated in both directions through the grain and linking themselves with the main crack.

It could be depicted that crack propagation of lamellar TiAl is always in a mixed mode (I + II) unless the crack is perpendicular to the lamellar orientation. When the crack reaches a grain boundary normal to the crack, it blunts first and then penetrates the grain with a zigzagging path with a deformation where mode I is dominant. Thus crack assumes different mode mixity as it meanders through different grains with different lamellar orientations. However at the end of the journey it always resorts to mode I propagation to failure. Figure 3.22 shows various examples.

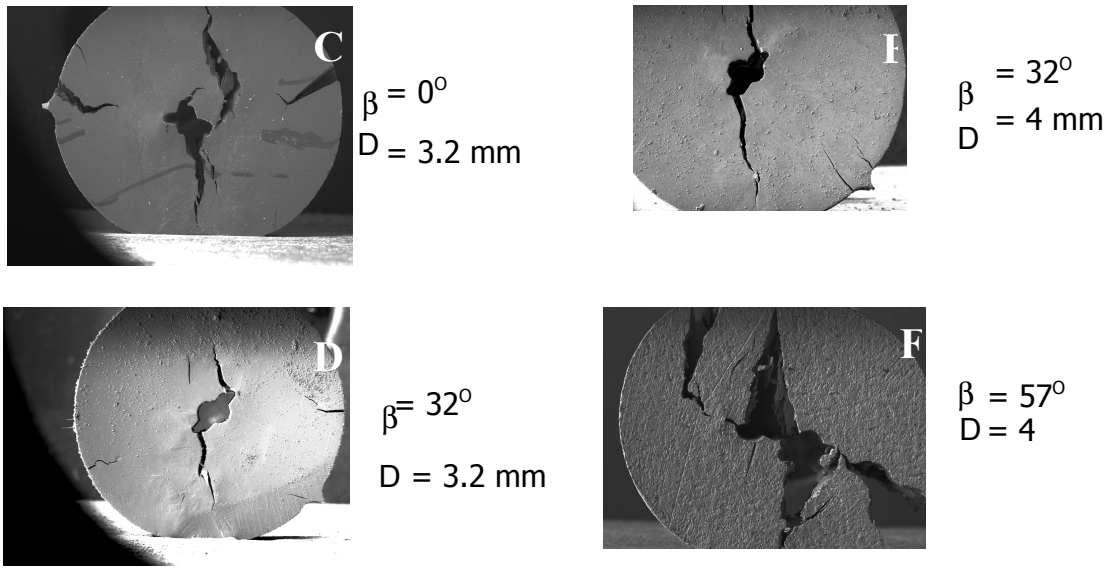


Figure3. 22 Mode I failure is the dominant failure mode irrespective of the initial Slot orientation.

Using the ESP we also able to evaluate the mode mixity from two representative displacement vectors on either side of the crack. An example is illustrated in Figure 3.23

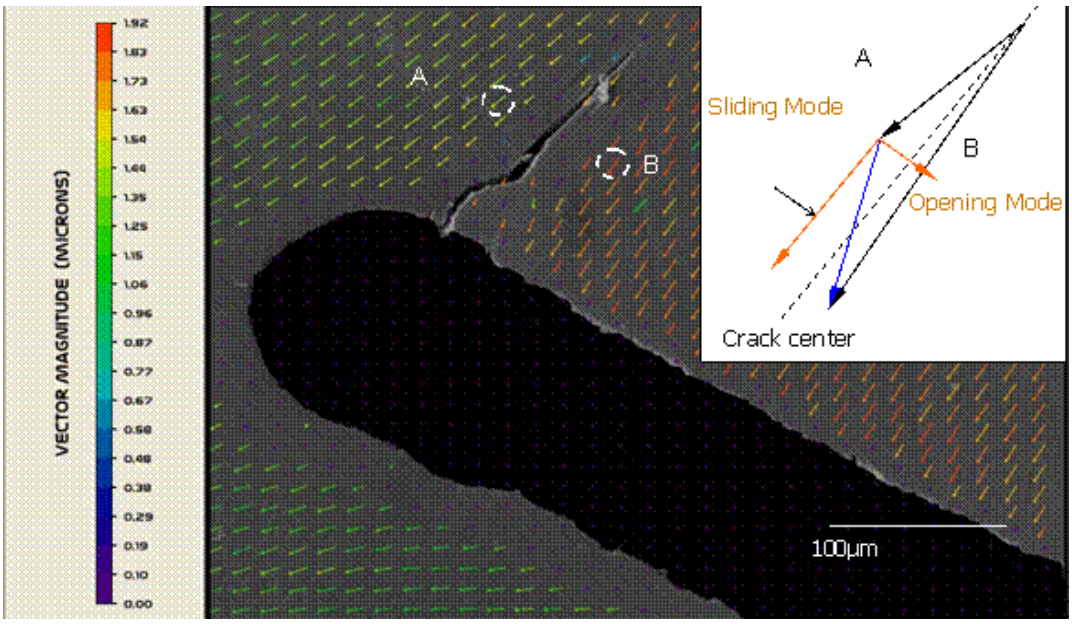


Figure3.23 Evaluation of mode mixity on CBD specimen

It can be concluded that electron speckle technique is an effective tool to study crack propagation characteristics. In TiAl the grain boundary retards the crack advance by providing large amount of resistance. The weakest path of the γ –α2 lamellar TiAl is the interface of the γ –α2 layers. When a crack runs into the junction of a cluster of grains with different orientation the crack seeks the γ –α2 interface which changes its direction from place to place. This act tends to retard the crack propagation. This phenomenon may explain why smaller grain TiAl compounds tend to have high fracture toughness. Smaller grains have many more grain boundaries for the crack to cross.

# Bibliography

**Appel,** F., Wagner, R., 1998, " Microstructure and deformation of two-phase γ-titanium aluminides", Materials *Science and Engineering*, R22 (1998) 187-268. **Vol.**22, pp.187-268

**Arata,** J.J.M., Needleman A., Kumar, K.S., Curtin, "Microcrack nucleation and growth in elastic lamellar solids", W.A., 2000, *International Journal of Fracture*, **Vol.**105, pp.321-342

**Chen**, D.J., Chiang, F.P., Tan, Y.S. and Don, H.S., 1993, *Applied Optics*, "Digital speckle-displacement measurement using a complex spectrum method", **Vol.**32 (11), pp.1839-1849

**Chiang**, F.P and Asundi, A., 1979, "White light speckle method of experimental strain analysis", *Applied Optics*, **Vol.**18, No.4, pp. 409-411

**Chiang**, F.P., 1978, *Solid Mechanics Archives*, "A New Family of2D and 3D Experimental Stress Analysis Techniques using Laser Speckles", **Vol.** 3 (1), pp.1-32

**Chiang**, F.P., 1989, *Metals Handbook*, 10th edition, **Vol.**17, pp.432-437

**Chan**, K.S., Kim**,** Y. W., 1992, *Metallurgical and Materials Transactions*, " Influence of microstructure on intrinsic and extrinsic toughening in an alpha-two titanium aluminide alloy" **Vol.**23A, pp.183-199

**Chan**, K.S., 1993, *Metallurgical and Materials Transactions*, "Toughening mechanisms in titanium aluminides", **Vol.**24A, pp.569

**Chan**, K.S., Kim, 1993, Y. W., "Rate and environmental effects on fracture of a two-phase TiAl-alloy", *Metallurgical and Materials Transactions*, **Vol.**24A, pp.113

**Chan**, K.S., Kim**,** Y. W., 1995, "Effects of lamellae spacing and colony size on the fracture resistance of a fully-lamellar TiAl alloy" *Acta Metallurgica et Materialia*, **Vol.**43-2, pp.439-451.

**Chan**, K.S., Kim**,** Y. W., 1994, "Relationships of slip morphology, microcracking, and fracture resistance in a lamellar TiAl-alloy", *Metallurgical and Materials Transactions*, **Vol.**25A, pp.1217

**Chan**, K.S., Shih, D., 1997, "Fatigue and fracture behavior of a fine-grained lamellar TiAl alloy", *Metallurgical and Materials Transactions*, **Vol.**28A, pp.79

**Chan**, K.S., Onstott, J., Kumar, S., 2000, "The fracture resistance of a binary TiAl alloy", *Metallurgical and Materials Transactions,* **Vol.**31A, pp.71

**Davidson** D.L. and Chan K.S., 1989, *Page: in Micromechanics: Experimental Techniques, ASME,* NY, **Vol.**102, pp.73-87

**Dimiduk**, D.M., Kim, Y.W., Wagner, R., Yamaguchi, M. (Eds.), 1995, *TMS*, Warrendale, PA., pp.3

**Feng,** C.R., Michel, D.J., Crowe, C.R., 1988, *Scripta Metallurgica et Materialia*, **Vol.**22, pp.1481

**Fett**, T., 2001, "Stress intensity factors and T -stress for internally cracked circular disks under various boundary conditions", *Engineering Fracture Mechanics*, **Vol.**68, pp.119–36

**Franke**, E.A, Wenzel, D.J., Davidson, D.L., 1991, "Measurement of microdisplacements by machine vision photogrammetry (DISMAP)", *Review of Scientific Instruments*, **Vol.** 62, pp.1270-79

**Inui,H**., Kishida, K., Misaki, M., Kobayashi, M., Shirai, M., Yamaguchi, M., 1995,

"Temperature dependence of yield stress, tensile elongation and deformation structures in polysynthetically twinned crystals of Ti-Al", *Philosophical Magazine,* **Vol.**A72, pp.1609

**Kim,** Y. W., 1994, Journal *of the Minerals, Metals and Materials Society*, **Vol.**46, pp.30

**Kim,** Y. W., 1995, "Effects of microstructure on the deformation and fracture of γ-TiAl alloys", *Material Science and Engineering*, **Vol.**A192/193, pp.519

**Peters**, W.H. and Ranson, W.F., 1982, "Digital Image Techniques in Experimental Stress Analysis", *Optical Engineering*, **Vol.**21, pp.427-431

**Sastry**, S.L.M., Lipsitt, H.A., 1977, "Fatigue deformation of TiAl base alloys", *Metallurgical and Materials Transactions*, **Vol.**8A, pp. 299

**Yao**, K.F., Inui,H., Kishida, K., Yamaguchi, M., 1995, "Plastic deformation of V- and Zr-alloyed PST TiAl in tension and compression at room temperature", *Acta Metallurgica et Materialia*, **Vol.**43, pp.1074

**Yamaguchi**, M.,Umakoshi, Y., 1990," The deformation behaviour of intermetallic superlattice compounds", *Progress in Materials Science*, **Vol.**34, pp.1

**Zupana** M. and Hemker K. J., 2001, "High temperature microsample tensile testing of γ-TiAl", *Materials Science and Engineering*, **Vol.**319, pp.810-814